

REPORT DOCUMENTATION PAGE

Form Approved OMB No. 0704-0188

Public reporting burden for this collection of information is estimated to average 1 hour per response, including the time for reviewing instructions, searching existing data sources, gathering and maintaining the data needed, and completing and reviewing the collection of information. Send comments regarding this burden estimate or any other aspect of this collection of information, including suggestions for reducing the burden, to Department of Defense, Washington Headquarters Services, Directorate for Information Operations and Reports (0704-0188), 1215 Jefferson Davis Highway, Suite 1204, Arlington, VA 22202-4302. Respondents should be aware that notwithstanding any other provision of law, no person shall be subject to any penalty for failing to comply with a collection of information if it does not display a currently valid OMB control number.

PLEASE DO NOT RETURN YOUR FORM TO THE ABOVE ADDRESS.

1. REPORT DATE (DD-MM-YYYY) 11-02-2010			2. REPORT TYPE Final Report	3. DATES COVERED (From – To) 1 April 2007 - 01-Apr-08	
4. TITLE AND SUBTITLE Ultra-Sensitive Mass Sensors Based on Suspended Carbon Nanotubes			5a. CONTRACT NUMBER FA8655-07-1-3086		
			5b. GRANT NUMBER		
			5c. PROGRAM ELEMENT NUMBER		
6. AUTHOR(S) Dr. Yuval E Yaish			5d. PROJECT NUMBER		
			5d. TASK NUMBER		
			5e. WORK UNIT NUMBER		
7. PERFORMING ORGANIZATION NAME(S) AND ADDRESS(ES) Technion Technion Haifa 32000 Israel			8. PERFORMING ORGANIZATION REPORT NUMBER N/A		
9. SPONSORING/MONITORING AGENCY NAME(S) AND ADDRESS(ES) EOARD Unit 4515 BOX 14 APO AE 09421			10. SPONSOR/MONITOR'S ACRONYM(S) 11. SPONSOR/MONITOR'S REPORT NUMBER(S) Grant 07-3086		
12. DISTRIBUTION/AVAILABILITY STATEMENT Approved for public release; distribution is unlimited.					
13. SUPPLEMENTARY NOTES					
14. ABSTRACT <p>This report results from a contract tasking Technion as follows: The primary goal of the proposed research is to take advantage of recent technological breakthroughs in the fields of nanomechanics and nano- and molecular-electronics in order to develop ultra-sensitive mass sensors, capable of detecting the mass of a single small molecule. Such sensors promise a broad range of applications, from ultra-sensitive mass spectrometers that can be used to detect hazardous molecules, through biological applications at the level of a single DNA base-pair, to the study of fundamental questions such as the interaction of a single pair of molecules. The proposed sensors are based on suspended nanomechanical resonators made out of carbon nanotubes, utilizing a unique combination of features that are available only at the nano-scale. The extremely small masses and high frequencies of vibration, the expected high quality factors, the low power consumption, the ability to take advantage of nonlinear behavior, and the ability to combine conventional top-down fabrication with self-assembled nanomaterials and molecular components in a single device, all hold the key to the successful achievement of our goal.</p>					
15. SUBJECT TERMS EOARD, Nanoelectronics, nanomechanics, Molecular Electronics					
16. SECURITY CLASSIFICATION OF: a. REPORT UNCLAS			17. LIMITATION OF ABSTRACT UL	18. NUMBER OF PAGES 39	19a. NAME OF RESPONSIBLE PERSON WYNN SANDERS, Maj, USAF
b. ABSTRACT UNCLAS					19b. TELEPHONE NUMBER (Include area code) +44 (0)1895 616 007

Ultra Sensitive Mass Sensors based on Suspended Carbon Nanotubes

Final research report of Yaish group

General

This project aims to utilize suspended Carbon Nanotube (NTs) as ultra sensitive mass sensors. For that purpose few steps had to be addressed. The most important and difficult mission was to fabricate suspended resonators made out of NTs which behave as field effect transistors (FETs) and posses noiseless and reproducible electrical characteristic. Without these requirements this project can't proceed. Therefore, first we developed and construct our own chemical vapor deposition (CVD) system. We design and build the plumbing for the machine and install it in our facilities. We succeed in operating it and receive high yield of single wall and multiwall NTs. We fabricate devices using these tubes and received FET behavior as expected. A huge effort was addressed in order to obtain straight and noiseless device. For that purpose we develop novel growth process, and study the various parameters that affect the growth outcome. Two kinds of lithography were implemented and different metal and annealing conditions were tested. At the end of this tedious process we succeed to obtain long, straight, and noiseless FET devices based on NTs. The next step was to design and build the experimental setup for the vibrational measurements. We designed and built three independent setups for these measurements and validate their operational capabilities. The first setup include high frequency room temperature vacuum chamber. The second consists of variable temperature vacuum insert, and the last is equipped with strong magnetic field. All three setups have been tested for operational at high frequencies up to \sim 1GHz. Equipped with experimental setup, the suspended resonators were fabricated. We designed and implemented three different paths for fabrication of suspended NTs, and all three of them exhibit promising results. The first method was based on suspending the NT up to its electrical contacts. In the second a trench was made on top of the NT and only portion of it was suspended. The last method was based on growing the NT above predefined trench. The best results that we obtain were based on the second method. However, higher quality factors are expected to be using the third method. Currently we pursue our research in this direction as well. For the second method we succeed to obtain the first few vibrational modes and receive wide range of mode tunability using external electric fields. We developed theoretical model for the experimental data with an excellent agreement. In addition, theoretical simulation of NT resonators was developed and several interesting prediction were found.

In addition to NTs, we developed novel technique to fabricate suspended Silicon Nanowires (SiNWs) that operate as FETs as well. This new approach is very important since it enables us to implement the same detection scheme for NT resonators to SiNWs as well. The chemistry of silicon surface is very reach and well established thus SiNW resonators offer us variety of optional antibody-antigen pairs for sensitive mass detection. Additionally, we studied how to attach various molecules onto the NT's surface. This capability is an important ingredient of this research proposal since enables us to attach specific molecules and thus obtain selective and sensitive mass sensor. There could be various means of attachment. The attachment can be very rigid and strong, as covalent bonding, but can be also looser, like Van der Waals interaction. We studied both regimes, since in advance it is not clear which type of connection is preferable for our application. Van der Waals interaction was

studied with deposition of the molecules over the final device. However, covalent bonding requires intensive research even before the final device is available. Therefore we decided to use amine chemistry in order to attach nanocrystal or small molecules onto the 1-dimesional wires. In practice we utilized this chemical reaction to attach gold colloid to the NTs.

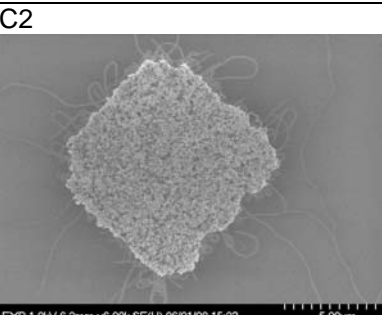
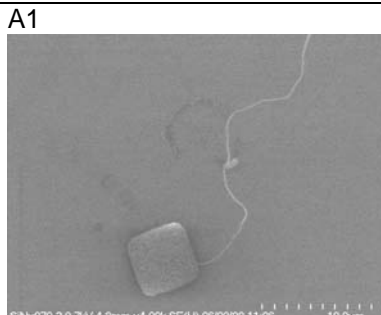
This final report is organized as follows:

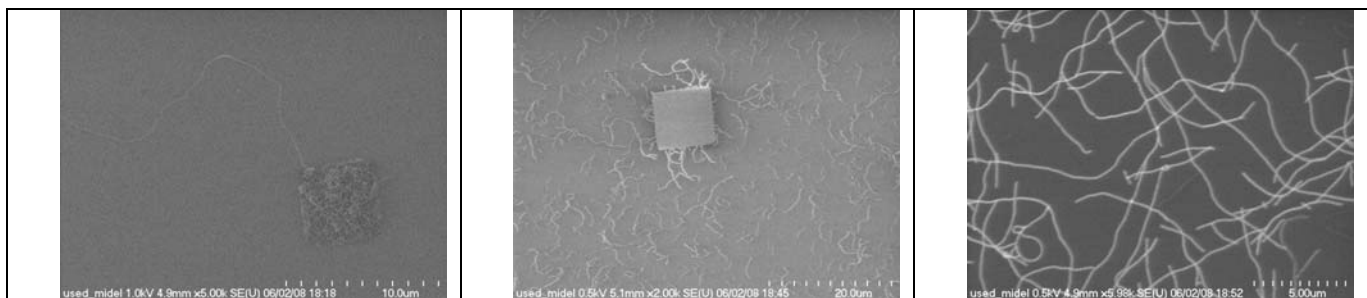
- Carbon nanotube growth
- FET fabrication
- Experimental setup
- Vibrational modes
- Theoretical simulation
- Silicon nanowires resonators
- Chemical modifications

Carbon nanotube growth:

In order to measure the vibration modes of suspended CNT we first had to fine-tune the growth process to achieve reasonable yield of SWNT longer than 20um and fairly straight, since curves usually mean defects in the CNT structure which tamper conductivity. Different recipes, catalysts, and substrate treatments were examined.

A summery of major modification and their results is listed below:

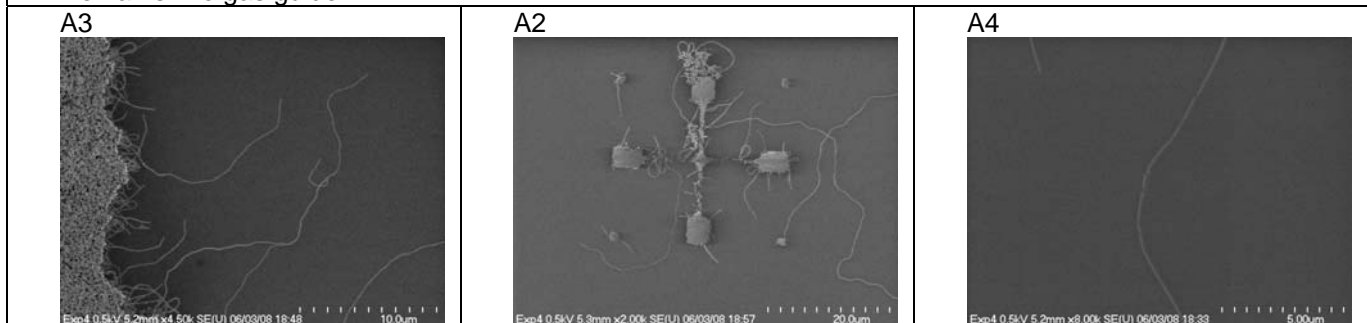
Recipe	<ol style="list-style-type: none"> 1. Heat to 750°C with 0.2 SLM Ar. 2. Reduction at to 750°C with 0.5 SLM H₂ and 0.5 SLM Ar at 600 Torr. 3. Heat to 850°C with 0.5 SLM H₂ 4. Growth at 850°C with 0.2 SLM H₂, 2 SLM CH₄ at 500 Torr. 10 minutes. 5. Cool down with 0.5 SLM H₂. 		
C2		A1	
Recipe	<ol style="list-style-type: none"> 6. Heat to 750°C with 0.2 SLM Ar. 7. Reduction at to 750°C with 0.5 SLM H₂ and 0.5 SLM Ar. 8. Heat to 900°C with 0.5 SLM H₂ 9. Growth at 900°C with 0.2 SLM H₂, 2 SLM CH₄ at 500 Torr. 10 minutes. 10. Cool down with 0.5 SLM H₂. 		
Remarks: No gas guide	A1	A2	A6



Recipe

1. Heat to 750°C with 0.2 SLM Ar.
2. Reduction at 750°C with 0.5 SLM H₂ and 0.5 SLM Ar at 600 Torr.
3. Heat to 900°C with 0.5 SLM H₂
4. Growth at 900°C with 0.2 SLM H₂, 2 SLM CH₄, 2 SLM Ar, at 500 Torr. 10 minutes.
5. Cool down with 0.5 SLM H₂.

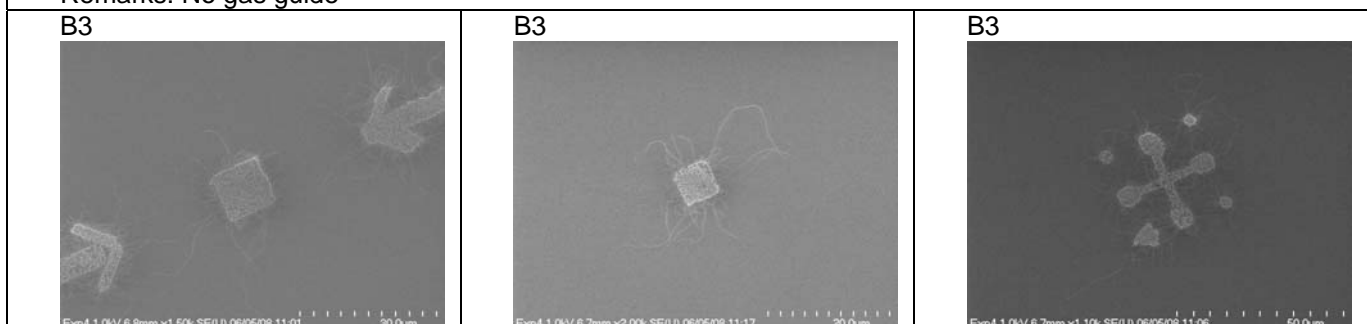
Remarks: No gas guide



Recipe

1. Heat to 900°C with 0.2 SLM Ar.
2. Growth at 900°C with 2 SLM CH₄ at 500 Torr. 10 minutes.
3. Cool down in vacuum.

Remarks: No gas guide



Recipe

1. Heat to 750°C with 0.2 SLM Ar.
2. Reduction at 750°C with 0.5 SLM H₂ and 0.5 SLM Ar at 600 Torr.
3. Heat to 900°C with 0.5 SLM H₂
4. Growth at 900°C with 2 SLM CH₄ at 500 Torr. 10 minutes.
5. Cool down in vacuum.

Remarks: No gas guide



(Flying Catalyst)

Recipe

1. Heat the oven in backward position to 900°C.
2. Growth at 900°C with 0.52 SLM CH₄, 0.7 SLM. Measure 10 minutes when the temperature reaches 820°C.

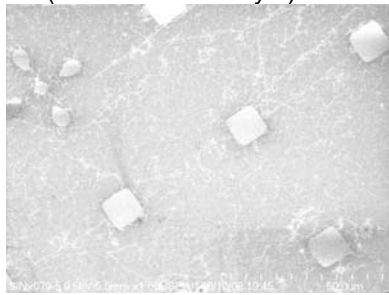
Remarks: No gas guide

Recipe

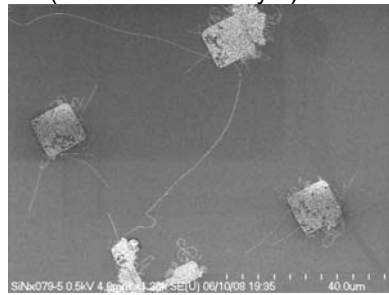
1. Heat the oven in backward position to 900°C.
2. Flow 0.52 SLM CH₄, 0.7 SLM H₂. Bring the furnace to forward position. Measure 10 minutes when the temperature reaches 820°C.
3. Pump the chamber and cool down with 0.1 SLM Ar.

Remarks: No gas guide

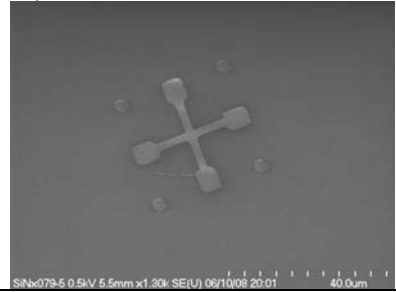
A4 (~2nm Fe + Catalyst)



A5 (~2nm Fe + Catalyst)



A2 (~2nm Fe + Fe NP low conc.)

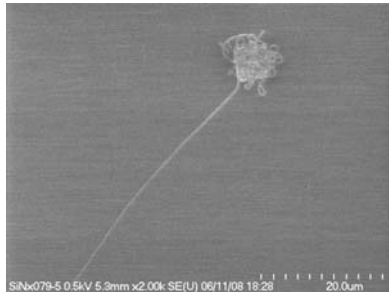


Recipe

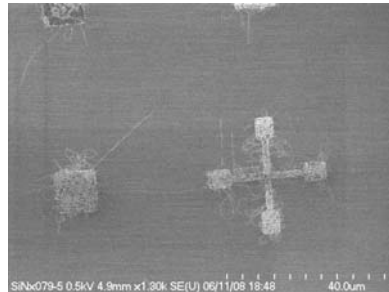
1. Heat the oven in backward position to 900°C.
2. Flow 2 SLM CH₄, 2 SLM H₂. Bring the furnace to forward position. Measure 10 minutes when the temperature reaches 820°C.
3. Pump the chamber and cool down with 0.1 SLM Ar.

Remarks: No gas guide

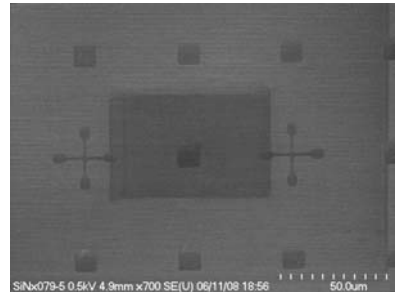
A5



A3



A1

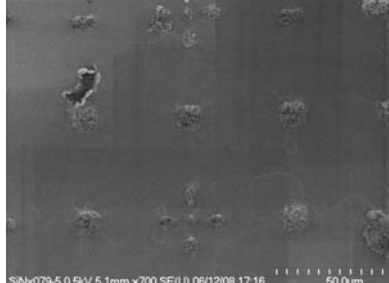


Recipe

1. Heat to 750°C in vacuum.
2. Reduction at 750°C with 0.5 SLM H₂ and 0.5 SLM Ar.
3. Bring furnace backward and cool down the chamber to 350°C.
4. Heat the furnace to 900°C.
5. Flow 2 SLM CH₄, 2 SLM H₂. Bring the furnace to forward position. Measure 10 minutes when the temperature reaches 820°C.

Remarks: No gas guide

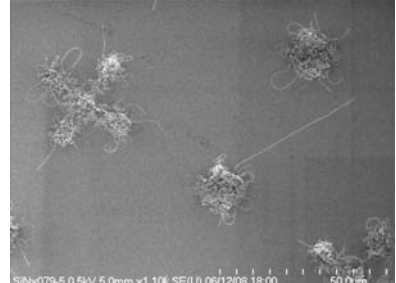
A3 (Fe NP)



A4 (Fe evaporation + Catalyst)



A5 (Catalyst)

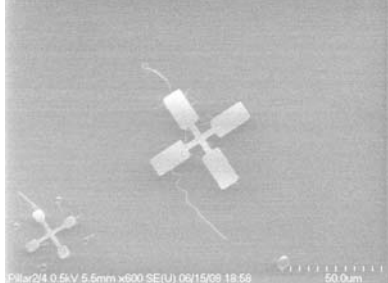


Recipe

1. Heat the oven in backward position to 900°C.
2. Flow 2 SLM CH₄, 2 SLM H₂. Bring the furnace to forward position. Measure 10 minutes when the temperature reaches 820°C.
3. Pump the chamber and cool down with 0.1 SLM Ar.

Remarks: No gas guide

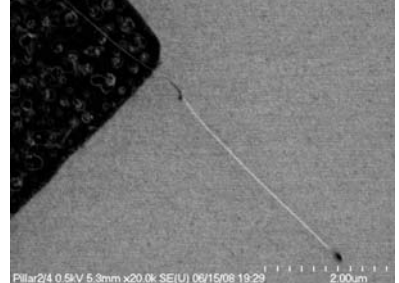
A1 (~2nm Fe)



A2 (~2nm Fe + catalyst)



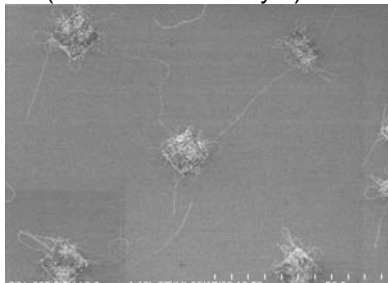
B1 (Ni evaporation)

**Recipe**

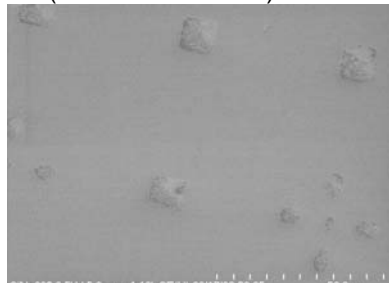
1. Heat the oven in backward position to 900°C.
2. Flow 1.2 SLM H₂
3. Flow 0.52 SLM CH₄, 0.7 SLM H₂. Bring the furnace to forward position. Measure 10 minutes when the temperature reaches 820°C.
4. Pump the chamber and cool down with 0.1 SLM Ar.

Remarks: No gas guide

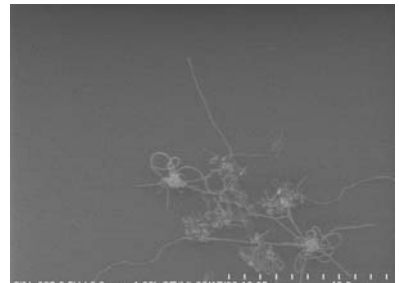
A3 (~2nm Fe + Catalyst)



A4 (Alumina + Fe NP)



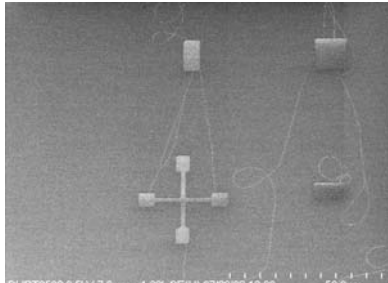
A2

**Recipe**

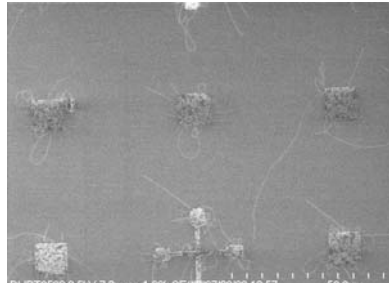
1. Heat the oven in backward position to 900°C.
2. Flow 0.52 SLM CH₄, 0.7 SLM H₂. Bring the furnace to forward position. Measure 10 minutes when the temperature reaches 820°C.
3. Pump the chamber and cool down with 0.1 SLM Ar.

Remarks: With gas guide

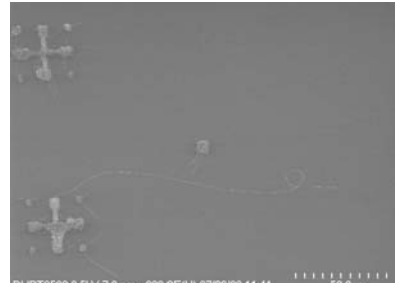
A1



A2



A3

**Recipe**

1. Heat the oven in backward position to 900°C.
2. Flow 0.52 SLM CH₄, 0.7 SLM H₂. Bring the furnace to forward position. Measure 10 minutes when the temperature reaches 820°C.
3. Pump the chamber and cool down with 0.1 SLM Ar.

Recipe

1. Heat the oven in backward position to 900°C.
2. Flow 0.52 SLM CH₄, 0.7 SLM H₂.
3. Bring the furnace to forward position. Retract the furnace at 500°C.

4. Pump the chamber and cool down with 0.1 SLM Ar.



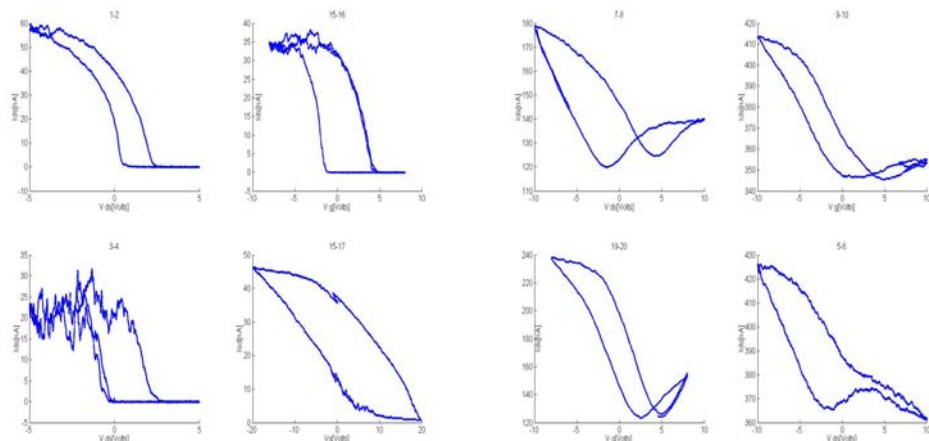
After huge amount of effort we have managed to repeatedly grow straight and long individual SWNT. Devices fabricated from these NT exhibited very low contact resistance (around 50 kOhm) and much better signal to noise ratio than devices fabricated from previously grown NTs.

Field Effect Transistor Fabrication:

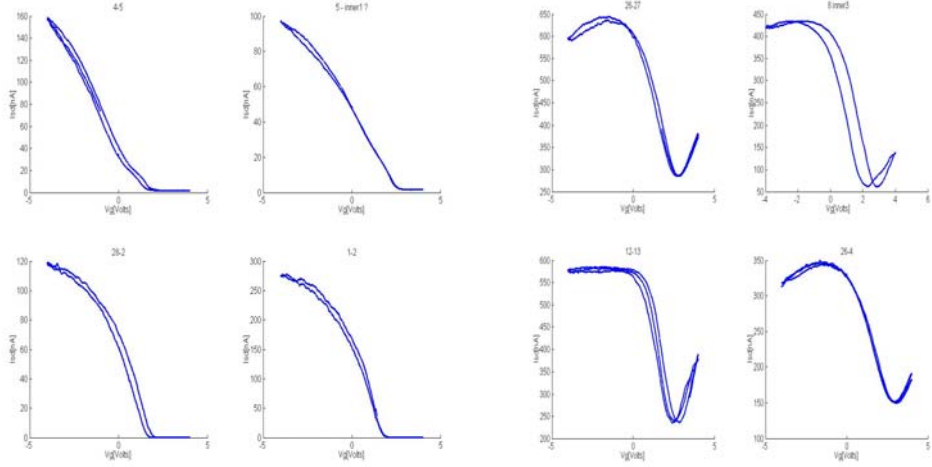
After growth optimization electrical contact were fabricated. Here, two methods have been used. The first was based on e-beam lithography, where each NT was addressed separately. The main advantage of this method is that each device is built from a single tube, and its length and diameter are known before completing the device. However, this method is very tedious, and difficult to utilize in order to study which for metal contact is better and what annealing conditions one should apply. The second method is based on optical lithography. We designed a clever mask in which after catalyst size and recipe optimization, statistically single NT is bridging between two nearby electrodes to form electrical contact. This procedure lack the knowledge how many NTs are connected between two electrodes, as well as their lengths and diameters. However, this information can be achieved after device fabrication, and the parallel process enable us to optimize growth recipes, metallic electrodes, and annealing conditions.

Below we present few electrical characteristics for NT FETs that were fabricated in our lab. In the first group, devices were made by e-beam lithography and in the last by photolithography.

SWNT FET-transistors made of semi-conducting cnt's (left) and small band gap cnt's (right) grown before optimal recipe with Cr/Au contacts.

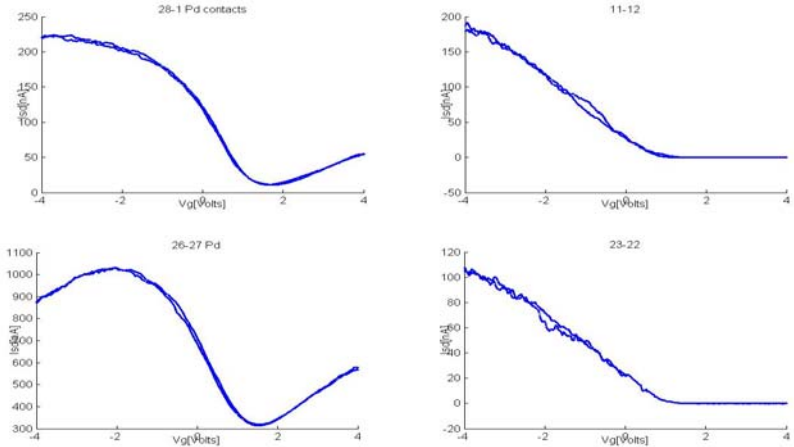


SWNT FET-transistors made of semi-conducting cnt's (left) and small band gap cnt's (right) grown with optimal recipe with Cr/Au contacts.

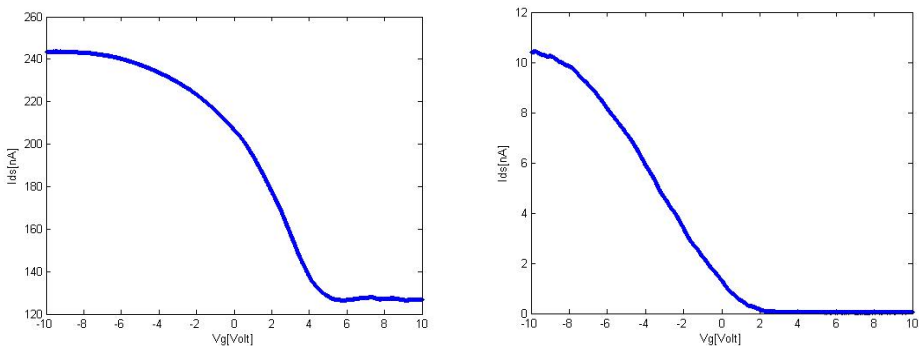


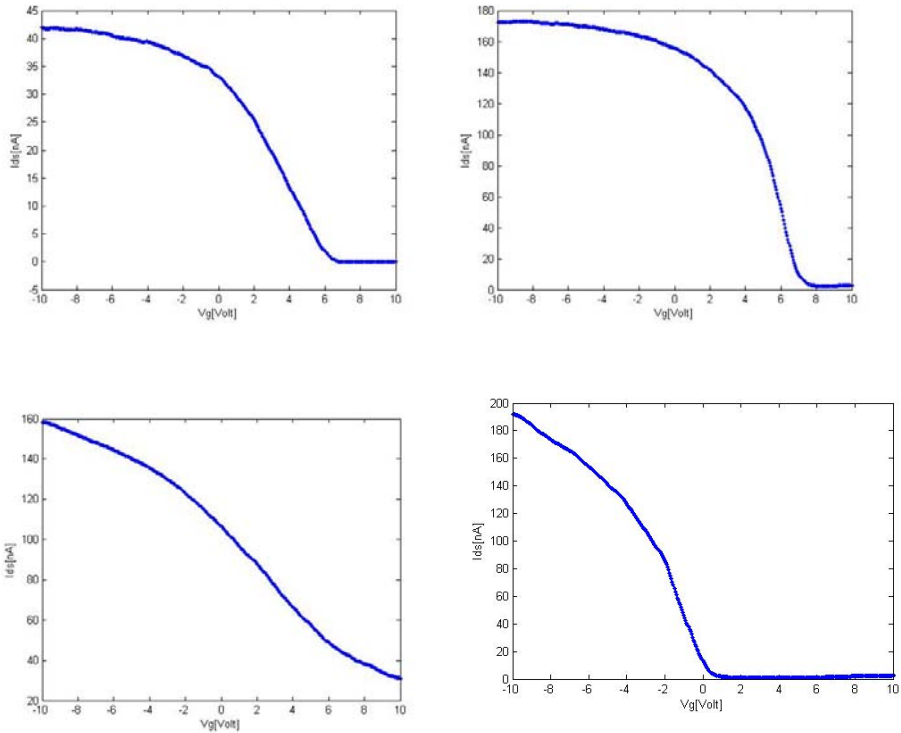
For the contact electrodes we have tries both Cr/Au (2nm/110nm) and Pd (30nm). Pd exhibited lower contact resistivity but devices were noisier (see below). An annealing step may solve this problem.

SWNT FET-transistors made of semi-conducting cnt's (right) and small band gap cnt's (left) grown with Pd contacts



These devices were made by e-beam lithography. The one below utilized photolithography procedure. In all of them Pd contact were deposited.





Since the yield per process of the photolithography path is much higher, it is easier to find long and noiseless NTs with compare to the e-beam method.

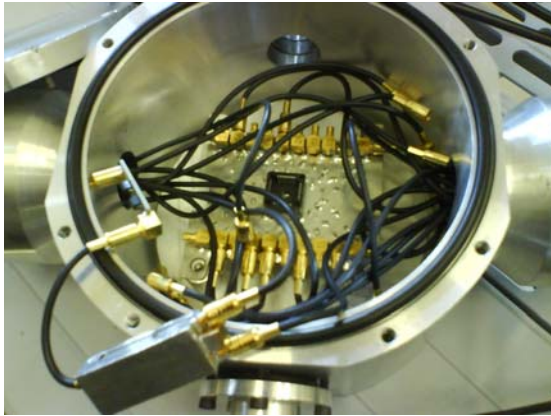
Experimental setup:

Two different measurement chambers were built for this measurement. The first is a Vacuum chamber with an option to introduce different gases. In the chamber sits a PCB which is connected to external co-ax cables via 28 SMB connectors. 2 different PCB were fabricated:

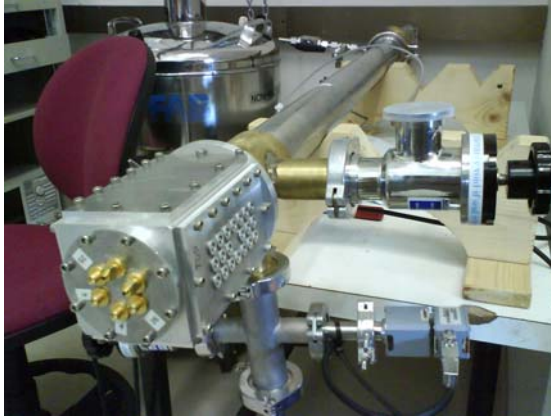
The first includes a 28 pin socket and transmission line designed for high frequency.

Half of the lines contain a 50ohm resistor in line with a 1nF capacitor which runs to ground just before the connection to the socket to avoid reflection of incoming wave due to the high impedance of the device. The PCB was tested to give reasonable signal up to frequencies of 500 MHz. A second PCB is identical to first one apart from the fact that it contains no socket. The sample is attached to the center of the PCB using a silver paint and the pads are directly bonded to the near-by PCB strip lines. This enables higher frequency measurements up to 800-900 MHz.

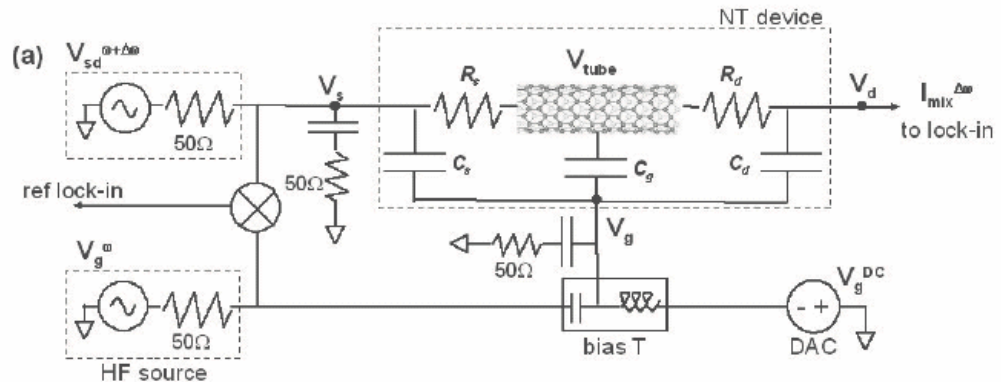
Picture of the Vacuum Chamber, Inner low noise amplifier and low pass filter



A second apparatus was built for cryogenic temperatures down to 4K. It is a dip-stick that can be cooled either by exchange gas or in high-vacuum using a cold-finger. In the bottom of dip-stick there is a socket identical to the one situated on the PCB of the vacuum chamber so samples can be interchanged. The socket is connected to 10 stainless-steel flexible coaxial cables, and 4 high frequency semi-rigid stainless steel cables. The flexible cables were tested to transmit signals up to 60 MHz and the semi-rigid up to 500MHz. The dip-stick temperature is controlled using an internal heater and a calibrated silicon diode for exact temperature measurements. The sample can be heated from 4K to 340K while in Dewar as was verified by a variator bonded to socket.



The measurement apparatus is as follows:



An RF signal with frequency ω_0 is fed into the source contact. A second RF signal with a frequency $\omega_0 - \Delta\omega$ is fed into the gate contact. The mixing term as explained

below is proportional to the derivative of the conductance (G) with respect to the gate voltage. The derivative of the conductance (G) with respect to the gate voltage can be compared with the numerical derivative of current versus gate voltage DC measurement. The gate capacitance (C_g) is a function of the NT's height above equilibrium (δz).

$$G = G(q)$$

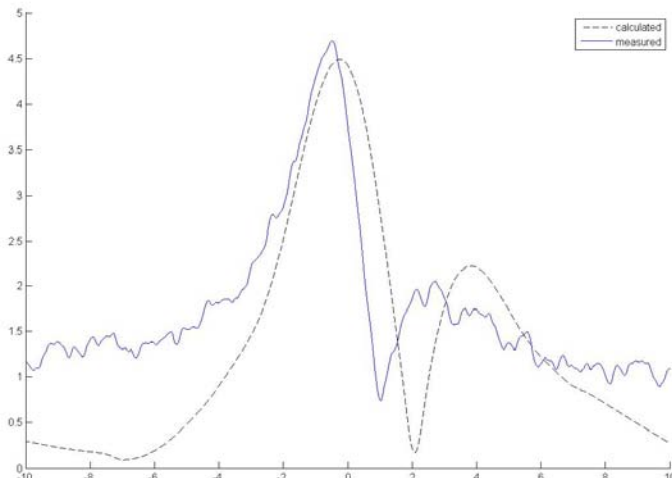
$$q = C_g(z)V_g$$

$$I_{SD} = V_{SD}G = (V_{SD}^{DC} + \tilde{V}_{SD}) \left(G \Big|_{V_g=V_g^{DC}, \delta z=0} + \frac{dG}{dq} \left(\frac{\partial q}{\partial z} \delta z + \frac{\partial q}{\partial V_g} \delta \tilde{V}_G \right) \right)$$

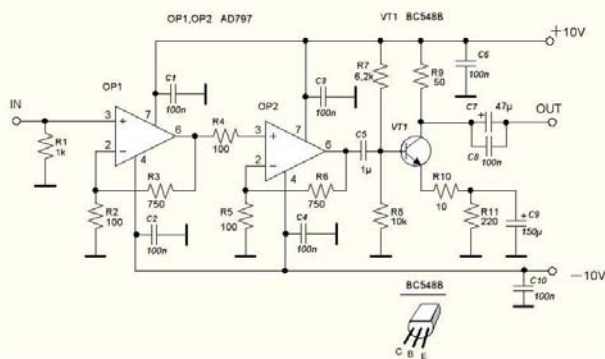
$$\delta \tilde{I}_{SD}^{\Delta \omega} = \frac{1}{2} \tilde{V}_{SD} \frac{dG}{dV_g} \Big|_{V_g=V_g^{DC}, \delta z=0} \left(\frac{C_g'}{C_g} V_g^{DC} \delta z(\omega) + \delta \tilde{V}_G \right)$$

In order to test the system we first made measurements with devices which are not suspended, thus the first term in the brackets of the last equation disappears. Comparing the numerical derivative and the mixed signal revealed that the signal is too noisy to measure the small signal from the mechanical vibrations.

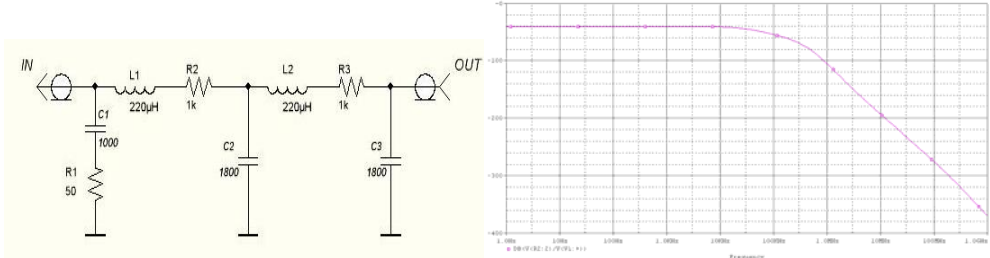
Measured Mixing signal taken at HF=10Mhz, IF=1kHz, Vgate(rms)=13mV, Vsd(rms)=10mv.



To solve the issue a low noise amplifier for the range of the intermediate frequency (300Hz-8MHz) was designed and built.

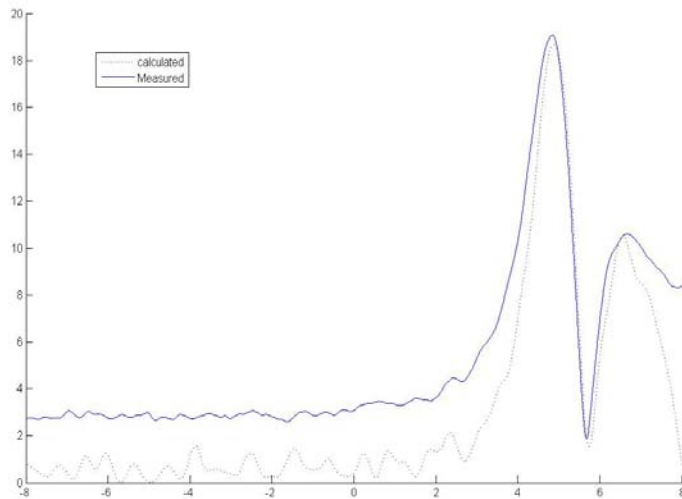


But the high frequency signal entering the amplifier saturated it and masked the signal. A 100dB Decade LPF just before the amplifier solved the issue.



The low-noise amplifier scheme (left) and its frequency response (right).

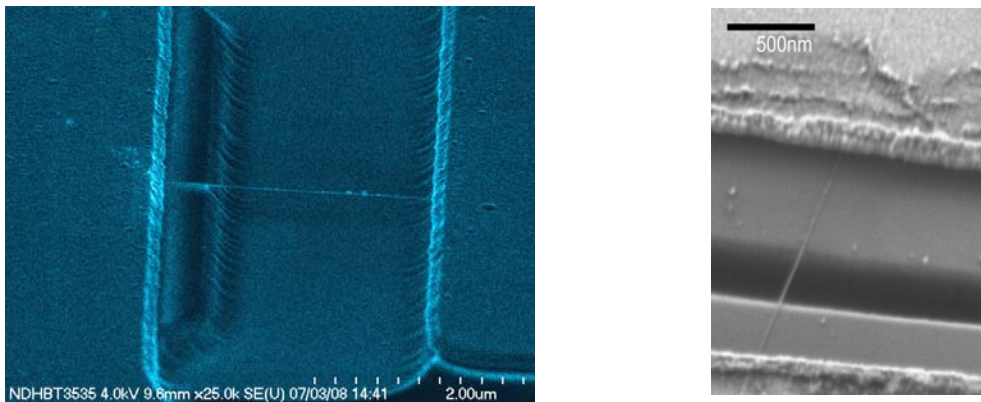
As can be seen the signal quality improved significantly.



Measured Mixing signal taken at HF=10MHz, IF=1kHz, Vgate(rms)=8mV, Vsd(rms)=6mV.

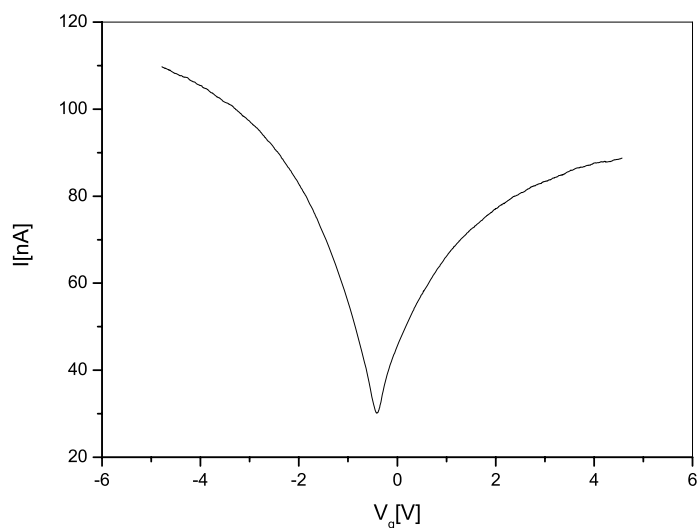
Suspended Device:

Once good devices were measured a second e-beam lithography stage defined trenches between the NT's electrodes. A wet etch and critical point drying process was utilized to remove 300nm and leave doubly clamped SWNT suspended above a trench. Alternatively pre-growth trench was defined and NT grows above the trench. Below are images of two suspended devices with these two different procedures.

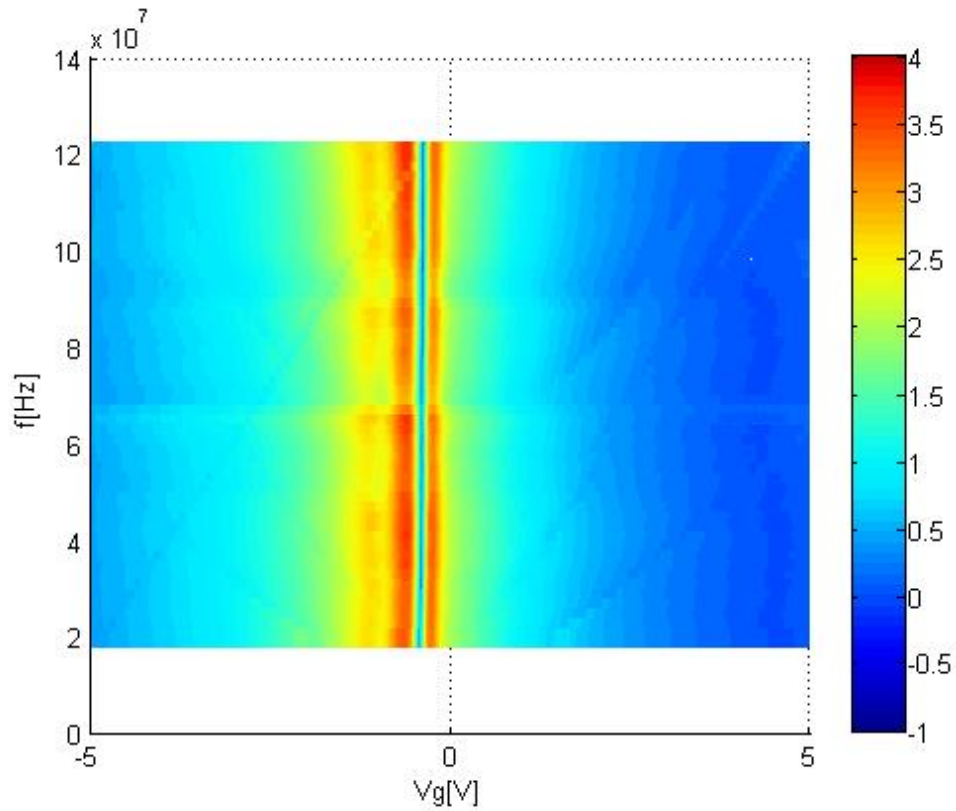


Vibrational modes:

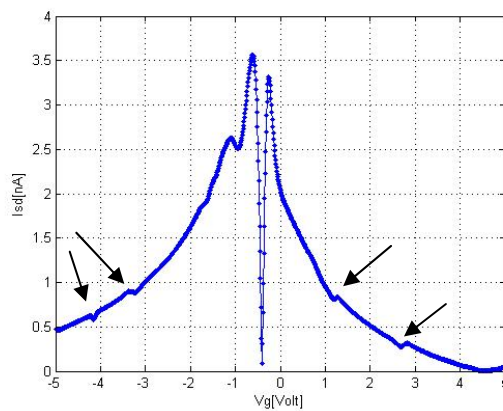
All the steps that we took in this research boil to the success of measuring the vibrational modes of suspended NTs. We succeed to measure few resonance frequencies of 2 micron length and 1.4nm diameter suspended NT. The electrical characteristics of this device were very quite, and posses small band gap semiconductor NT behavior.



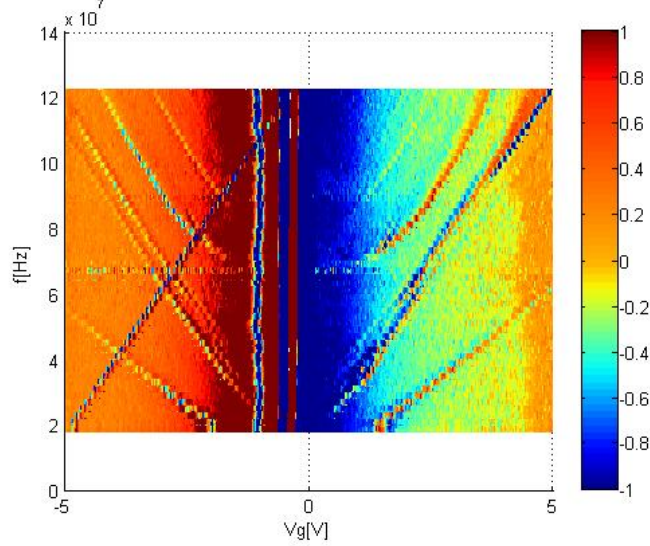
When introduce into the vacuum chamber and perform our mixing experiment the following graph was obtained. The x-axis represents the dc gate voltage that may tune the tube and hence modify its resonance frequencies, and the y-axis represents the resonance frequencies. The different colors present the tube conductance.



One can notify the dim contour that have parabolic shape and extend from low to high frequency as the gate voltage increases. A cut along the x-axis is plotted below. The arrows point on the resonance frequencies of this tube.



In order to enhance the visibility of these lines, derivative with respect to gate voltage is plotted below.



Now, one can see very easily the dispersion curves of the vibrational frequencies. In order to develop theoretical model for these resonances one should address very carefully all the factors that affect these modes. More specifically, the current along the NT is

$$\begin{aligned}
 I &= G \cdot V_{sd} \\
 \delta I &= \frac{\partial G}{\partial q} \delta q \cdot \delta V_{sd}(t) \\
 \delta q &= C_g \delta V_g(t) + V_g \delta C_g \\
 \delta V_{sd}(t) &= \delta V_{sd} \cdot \cos(\omega_1 t + \varphi_1) \\
 \delta V_g(t) &= \delta V_g \cdot \cos(\omega_2 t + \varphi_2) \\
 \delta C_g(t) &= \frac{\partial C_g}{\partial z} \delta z(t)
 \end{aligned}$$

All together we get

$$\begin{aligned}
 \delta I &= \frac{1}{C_g} \frac{\partial G}{\partial V_g} \cdot (C_g \delta V_g(t) + V_g \delta C_g(t)) \cdot \delta V_{sd}(t) \\
 &= \frac{1}{C_g} \frac{\partial G}{\partial V_g} \cdot (C_g \delta V_g(t) + V_g \frac{\partial C_g}{\partial z} \delta z(t)) \cdot \delta V_{sd}(t)
 \end{aligned}$$

The current expression contains $\delta z(t)$. In order to know $z(t)$ we need to calculate the force. After, we can solve the differential equation for forced and damped harmonic oscillators. The force that acts on the NT is:

$$F = \frac{1}{2} \frac{\partial C_g}{\partial z} (V_g^{DC} + \delta V_g(t) - \delta V_{sd}(t))^2$$

Since the DC term is much bigger than the AC term we can approximate it to

$$F = \frac{1}{2} \frac{\partial C_g}{\partial z} ((V_g^{DC})^2 + 2V_g^{DC} (\delta V_g(t) - \delta V_{sd}(t)))$$

Now we can solve the harmonic equation:

$$m \cdot \ddot{z} + \Gamma \cdot \dot{z} + k \cdot z = \frac{\partial C_g}{\partial z} V_g^{DC} \cdot (\delta V_g \cdot \cos(\omega_2 t + \varphi_2) - \delta V_{sd} \cdot \cos(\omega_1 t + \varphi_1))$$

For conventional geometry where the NT is suspended above planar gate the capacitance is given by

$$C_g = \frac{2\pi\epsilon_0}{\ln(2z/r)}$$

$$\frac{\partial C_g}{\partial z} = -C_g \cdot \frac{1}{z \ln(2z/r)}$$

When solving the harmonic equation one finds $\delta z(t) = A \cdot \cos(\omega t + \varphi)$ and the current is

$$\delta I = \frac{\partial G}{\partial V_g} \cdot (\delta V_g \cos(\omega_2 t + \varphi_2) - V_g^{DC} \frac{1}{z \ln(2z/r)} A \cos(\omega t + \varphi)) \cdot \delta V_{sd} \cos(\omega_1 t + \varphi_1)$$

In the lockin this term is multiply by $\cos((\omega_1 - \omega_2)t + \varphi_3)$ and we perform an integral over $2\pi/(\omega_1 - \omega_2)$. Lets find the solution for $\delta z(t)$. We ignore for the moment that the force term has two frequencies and assume we need to find solution for the following equation

$$m \ddot{z} + \Gamma \dot{z} + kz = f_0 \cdot \cos(\omega t + \varphi)$$

The solution is

$$z(t) = \frac{f_0}{\sqrt{m^2(\omega_0^2 - \omega^2)^2 + (\Gamma\omega)^2}} \cdot \left\{ \frac{m(\omega_0^2 - \omega^2)}{\sqrt{m^2(\omega_0^2 - \omega^2)^2 + (\Gamma\omega)^2}} \cos(\omega t + \varphi) + \frac{\Gamma\omega}{\sqrt{m^2(\omega_0^2 - \omega^2)^2 + (\Gamma\omega)^2}} \sin(\omega t + \varphi) \right\}$$

$$= \frac{f_0}{\sqrt{m^2(\omega_0^2 - \omega^2)^2 + (\Gamma\omega)^2}} \cdot \cos(\omega t + \varphi - \varphi(\omega)) \quad (2)$$

where we use the relation $\cos(a - b) = \cos(a) \cos(b) + \sin(a) \sin(b)$ and

$$\cos(\varphi(\omega)) = \frac{m(\omega_0^2 - \omega^2)}{\sqrt{m^2(\omega_0^2 - \omega^2)^2 + (\Gamma\omega)^2}}$$

$$\sin(\varphi(\omega)) = \frac{\Gamma\omega}{\sqrt{m^2(\omega_0^2 - \omega^2)^2 + (\Gamma\omega)^2}}$$

Also we have

$$\tan(\varphi(\omega)) = \frac{\Gamma\omega}{m(\omega_0^2 - \omega^2)}$$

If $\omega_0 - \omega \ll \omega_0$ one finds

$$m^2(\omega_0^2 - \omega^2)^2 + (\Gamma\omega)^2 \approx 4m^2\omega_0^2((\omega_0 - \omega)^2 + \Gamma^2/4m^2) = 4m^2\omega_0^4((1 - \omega/\omega_0)^2 + (\Gamma/2m\omega_0)^2)$$

If we define

$$G(\omega) = 1/\sqrt{(1 - \omega/\omega_0)^2 + (\Gamma/2m\omega_0)^2}$$

we see that if we take the square of it we get
 $G(\omega) = 1/((1 - \omega/\omega_0)^2 + (\Gamma/2m\omega_0)^2)$.

So the width of the lorentian is

$$\omega_{up} - \omega_{down} = \delta\omega = \frac{\Gamma}{m} = \frac{\omega_0}{Q}$$

and we get

$$G(\omega) = 1/\sqrt{(1 - \omega/\omega_0)^2 + (1/2Q)^2}$$

$$\tan(\varphi(\omega)) = \frac{\Gamma\omega}{m(\omega_0^2 - \omega^2)} \approx \frac{1}{2Q(1 - \omega/\omega_0)}$$

At the end we can write

$$z(t) = \frac{f_0}{2k} G(\omega) \cos(\omega t + \varphi - \varphi(\omega))$$

Since we have excitation from the source and from the drain we can find solution of the form of linear superposition of the two independent solutions, meaning:

$$z(t) = \frac{f_g}{2k} G(\omega_g) \cos(\omega_g t + \varphi_g - \varphi_g(\omega)) + \frac{f_{sd}}{2k} G(\omega_{sd}) \cos(\omega_{sd} t + \varphi_{sd} - \varphi_{sd}(\omega))$$

The expression for the current is:

$$\begin{aligned} \delta I &= \frac{\partial G}{\partial V_g} (\delta V_g \cos(\omega_g t + \varphi_g) - \\ &\quad \frac{V_g}{z \ln(2z/r)} (\frac{f_g}{2k} G(\omega_g) \cos(\omega_g t + \varphi_g - \varphi_g(\omega)) + \frac{f_{sd}}{2k} G(\omega_{sd}) \cos(\omega_{sd} t + \varphi_{sd} - \varphi_{sd}(\omega))) \\ &\quad \cdot \delta V_{sd} \cos(\omega_{sd} t + \varphi_{sd})) \end{aligned} \quad (3)$$

Let's give expression for f_g and f_{sd} :

$$f_g = \frac{\partial C_g}{\partial z} V_g^{DC} \delta V_g = -C_g \frac{V_g^{DC}}{z \ln(2z/r)} \delta V_g$$

$$f_{sd} = -\frac{\partial C_g}{\partial z} V_g^{DC} \delta V_{sd} = C_g \frac{V_g^{DC}}{z \ln(2z/r)} \delta V_{sd}$$

If we plug these expressions and use the following relation, $\cos(a) \cos(b) = 1/2 \cos(a + b) + 1/2 \cos(a - b)$, and looks at the low frequencies terms, the current looks like

$$\begin{aligned} \delta I &= \frac{1}{2} \frac{\partial G}{\partial V_g} \delta V_g \delta V_{sd} \{ \cos((\omega_g - \omega_{sd})t + \varphi_g - \varphi_{sd}) + \\ &\quad (\frac{V_g^{DC}}{z \ln(2z/r)})^2 [\frac{C_g}{2k} G(\omega_g) \cos((\omega_g - \omega_{sd})t + \varphi_g - \varphi_g(\omega) - \varphi_{sd}) \\ &\quad - \frac{C_g}{2k} G(\omega_{sd}) \cos(\varphi_{sd} - \varphi_{sd}(\omega) - \varphi_{sd})] \} \end{aligned}$$

We can multiply with the reference signal in the Lock-In $\cos((\omega_g - \omega_{sd})t)$ and perform integral over few periods. It is important to understand what the lockin does: The lockin receives the reference signal and we always have the freedom to say that the phase is zero. Then it multiplies the input signal with $\cos(\omega t)$ and $\sin(\omega t)$ and perform integral over few periods of the oscillations.

If we assume that the signal is $A \cos(\omega t + \varphi)$, one finds:

$$\frac{1}{T} \int_0^T A \cos(\omega t + \varphi) \cos(\omega t) = \frac{A}{2} \cos(\varphi)$$

$$\frac{1}{T} \int_0^T A \cos(\omega t + \varphi) \sin(\omega t) = -\frac{A}{2} \sin(\varphi)$$

Combine these results together, the expression for the current will be given by:

$$\delta I = \frac{1}{2} \frac{\partial G}{\partial V_g} \delta V_g \delta V_{sd} \{ \cos(\varphi_g - \varphi_{sd}) + \left(\frac{V_g^{DC}}{z \ln(2z/r)} \right)^2 \frac{C_g}{2k} G(\omega_g) \cos(\varphi_g - \varphi_g(\omega) - \varphi_{sd}) \}$$

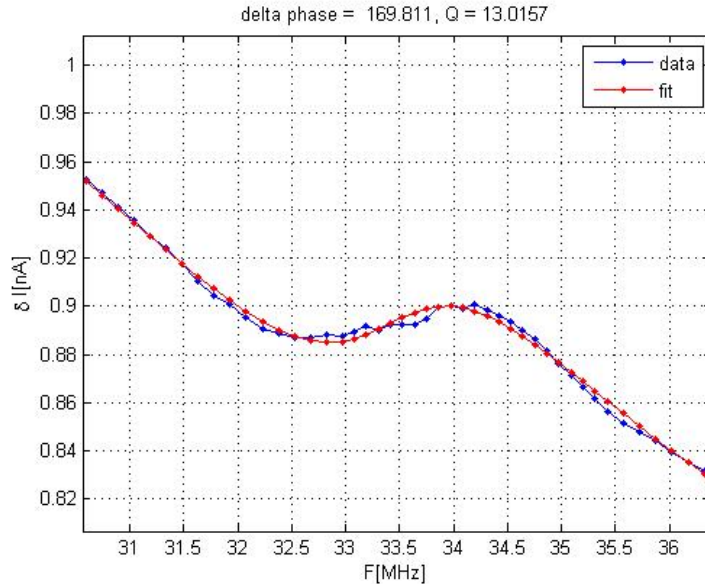
If Q is not too big one need to use the following equations:

$$GG(\omega) = 1 / \sqrt{(1 - (\omega/\omega_0)^2)^2 + (\omega/\omega_0 Q)^2}$$

$$\tan(\varphi(\omega)) = \frac{\Gamma\omega}{m(\omega_0^2 - \omega^2)} = \frac{\omega_0\omega}{Q(\omega_0^2 - \omega^2)}$$

$$\delta I = \frac{1}{2} \frac{\partial G}{\partial V_g} \delta V_g \delta V_{sd} \{ \cos(\varphi_g - \varphi_{sd}) + \left(\frac{V_g^{DC}}{z \ln(2z/r)} \right)^2 \frac{C_g}{k} GG(\omega_g) \cos(\varphi_g - \varphi_g(\omega) - \varphi_{sd}) \}$$

Having these formulas one can fit the experimental data to this model. The result of the fitting of the first vibrational mode is depicted below:



As we can see, the agreement between theory and experiment is excellent. The calculated quality factor is $Q \sim 13$, which is quite low for this setup. Others modes have

similar Q, up to 30. This low Q is a result of the suspension process. Currently we developed novel approach in order to overcome this obstacle. From the fitting one can extract also δz and the applied force. It turns out that $\delta z \sim 10\text{nm}$ and $\delta f \sim 1\text{fN}/\sqrt{\text{Hz}}$. These values are not the minimum detection sensitivities of this resonator and measurement of these values are still in progress.

Atomistic Simulations of Nano-Electro-Mechanical Systems Based on Carbon Nanotubes.

The primary goal of the proposed research is to take advantage of recent technological breakthroughs in the fields of nanomechanics and nano- and molecular-electronics in order to study suspended nano-electro-mechanical resonators based on Carbon Nanotubes (NTs) [4]. We plan to develop a theoretical understanding of dissipation processes and nonlinear dynamics in these resonators which will help the experimentalists utilize them as ultra-sensitive mass and force sensors. Specifically, we intend to study the dependence of the frequency and mode shape on the resonator quality factor, and to design it for optimal operation. Currently, the conventional NEMS have the advantage of having higher quality factors, higher demonstrated resonance frequencies (1GHz), better frequency stability, and easier on-chip integration, while NTs possess extremely-small masses and therefore hold the potential of becoming the ultimate mass sensors once their remaining properties have been optimized.

Results

We have begun atomistic simulations to generate data for the SWCNT vibrations in order to find and tune the frequencies to obtain improved sensitivity of NT devices. We started with a small model of a 98.38 Å armchair nanotube with a diameter of 9.4 Å and a chiral vector of (7,7) clamped at both ends using the Brenner interatomic potential [5].

Our first numerical experiments are monitoring thermal vibrations of such a NT at 300K. We let the nanotube vibrate during 626 psec with a time step of 0.5 fsec. The center of mass for each period of the nanotube (28 atoms in each period), see Fig. 3, was calculated (red dots/dark gray in Figure 4), we call this line of points the Centered Axis (CA). We analyzed the vibrations of the CA at a point near the center of mass of the nanotube with clamped ends (3 periods at each end do not move). The tube axis is in the Y direction, X and Z are perpendicular (see Figure 4). This nanotube has 40 periods and the center of mass (CM) of entire tube is near Y = 20.

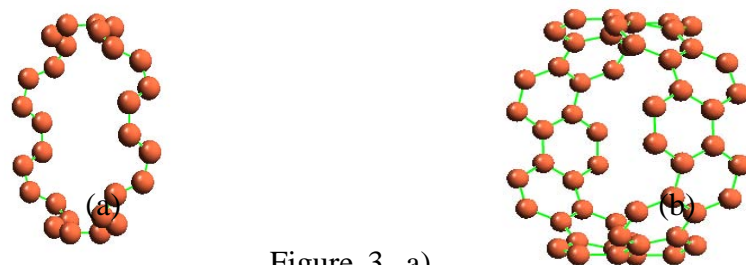


Figure 3. a)
one period; b)

two periods of a (7,7) Single Walled Carbon Nanotube.

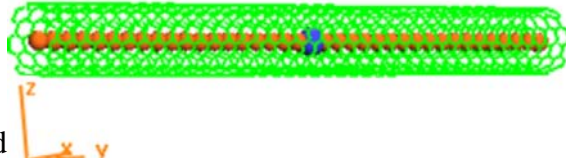


Figure 4. Single walled Carbon Nanotube (green/light gray), center of mass (CM) for each period of nanotube (red/dark gray), blue/dark gray atom in the center indicates CM of the nanotube.

In order to see the first four frequencies (including $n = 2$ and $n = 4$) we monitored the amplitude near the CM of the nanotube vs. time of the vibration (time domain) and from the Fourier Transform (FT) analysis the amplitude vs. frequency (frequency domain). Longer SWCNTs were tested and demonstrated the $f \sim L^{-2}$ dependency, where f is the frequency, L is the length of the nanotube, as was theoretically expected.

First, we wanted to test the reliability of the method of Fourier Transform for the mode's frequency decomposition. We let the nanotube vibrate 10 times longer than the period (T) of the lowest mode ($n = 1$). The vibration of the CM of the nanotube in Z direction is presented in Fig. 5 and the frequencies in Fig. 6, this figure demonstrates that the frequencies of the first modes can be distinguished with good resolution.

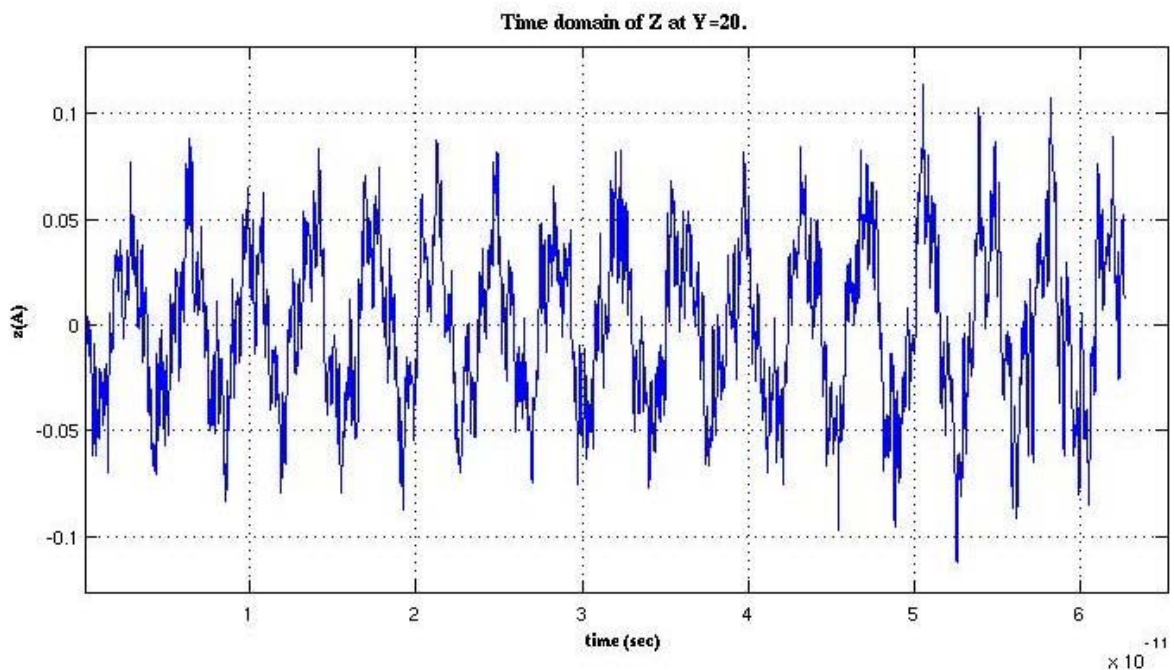
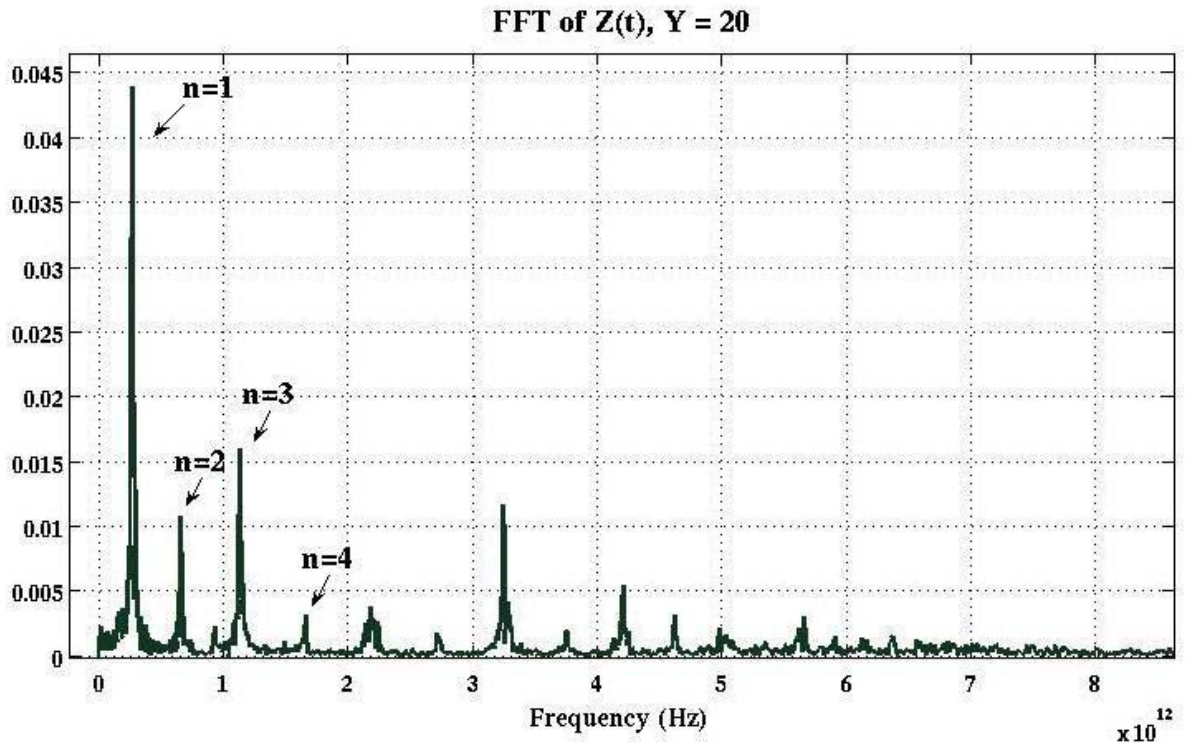


Figure 5. Time domain of the thermal vibrations of the CM in the Z direction at 300K.

We also observe in Fig.6 that the amplitude of the first mode ($n = 1$) has a high value, however the amplitude of the second mode ($n = 2$) is lower than that of the

third mode ($n=3$). This is obvious because, since the center of mass of 20th period of the nanotube is near the CM of the nanotube (the distance being about 1.42Å), which does not move in the second and fourth modes, its amplitude is low (see Fig. 7 for the



modes of vibrations).

Figure 6. Frequency domain of the thermal vibrations of the CM in Z direction at 300K.

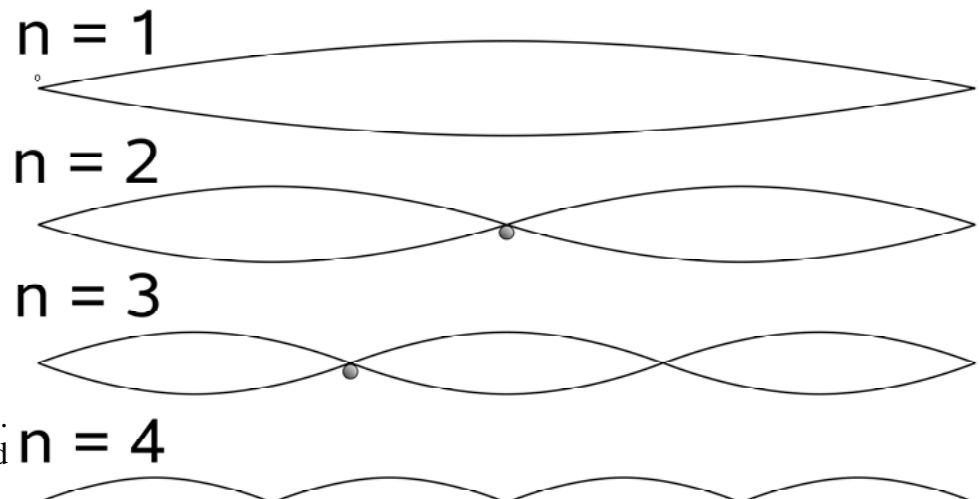


Figure 7.
Vibration and standing waves: the fundamental and the first 3 overtones ($n = 1, \dots, 4$).

We compared our results to frequencies which were calculated analytically from a continuum model [6] as presented in Table 1. Since we treat a 98.38Å nanotube,

which is clamped at both ends (3 periods at each end), the length of the vibrating part of the nanotube is 98.38A minus length of the 6 periods, which do not move, and equal to 83.62A.

Table1. Analytically calculated and simulated frequencies in THz. t is the wall thickness, $\square_1 = 1.300 \text{ g/cm}^3$ and $\square_2 = 9.517 \text{ g/cm}^3$.

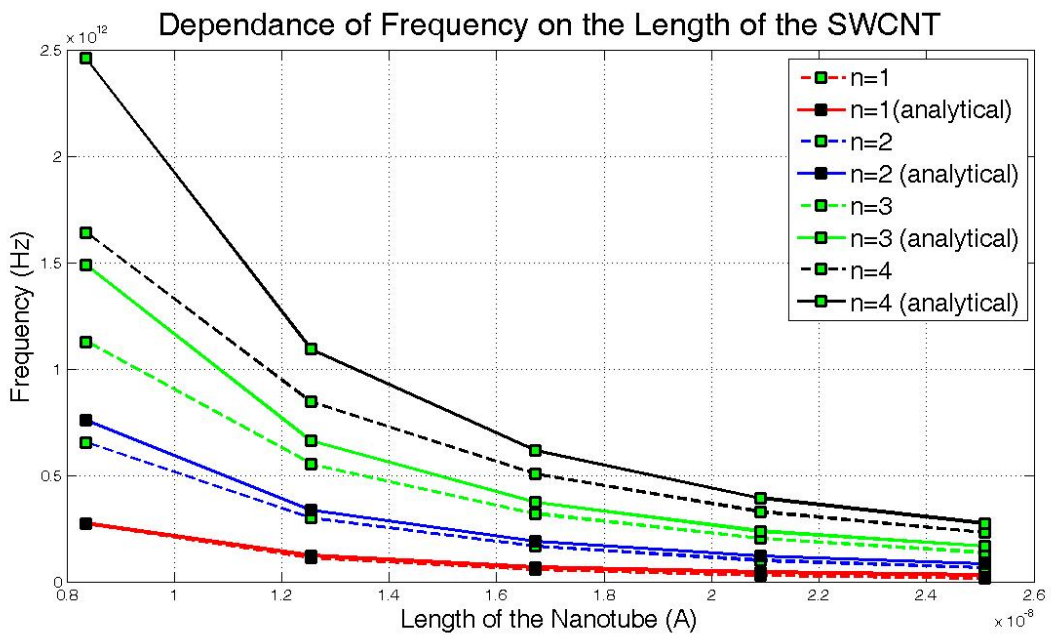
n	1	2	3	4
Simulated	0.269	0.659	1.130	1.660
ρ_1	0.279	0.770	1.510	2.500
$t=0.34\text{nm}$	3.6	14.4	25.2	33.6
ρ_2	0.213	0.586	1.150	1.900
%error	26.3	12.5	1.7	12.6
Con				

sidering only the continuum model with density $\square_1 = 1.300 \text{ g/cm}^3$, which is a more realistic density, the first mode is in excellent agreement with the simulations. The error of simulated frequencies vs. analytically calculated ones increases with n . We still need to investigate this effect, but think that the reason may be the nanometric scale effects which may change the elastic properties of the SWCNT. It is important to note, that in the analytic model a constant value of the Young's modulus of 1 TPa was taken for the calculations.

To be more specific a detailed graphs are present below.

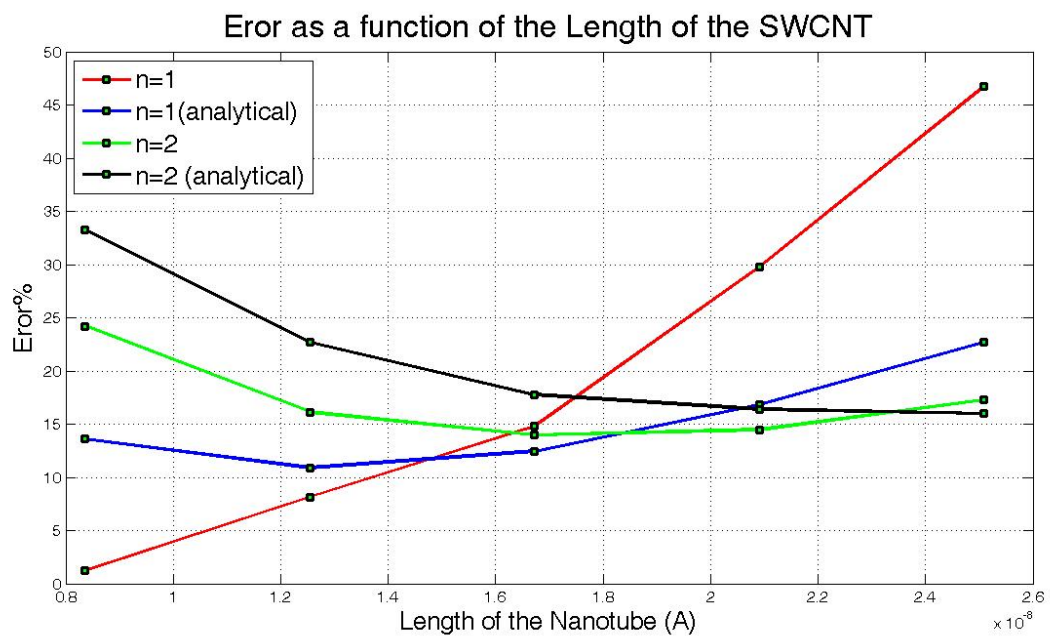
1. We have calculated the vibrations of the longer (7,7) nanotubes:

$R = 4.72\text{A}$; nanotubes of 83.62A, 125.43A, 167.24A and 209.05A, 40, 60,

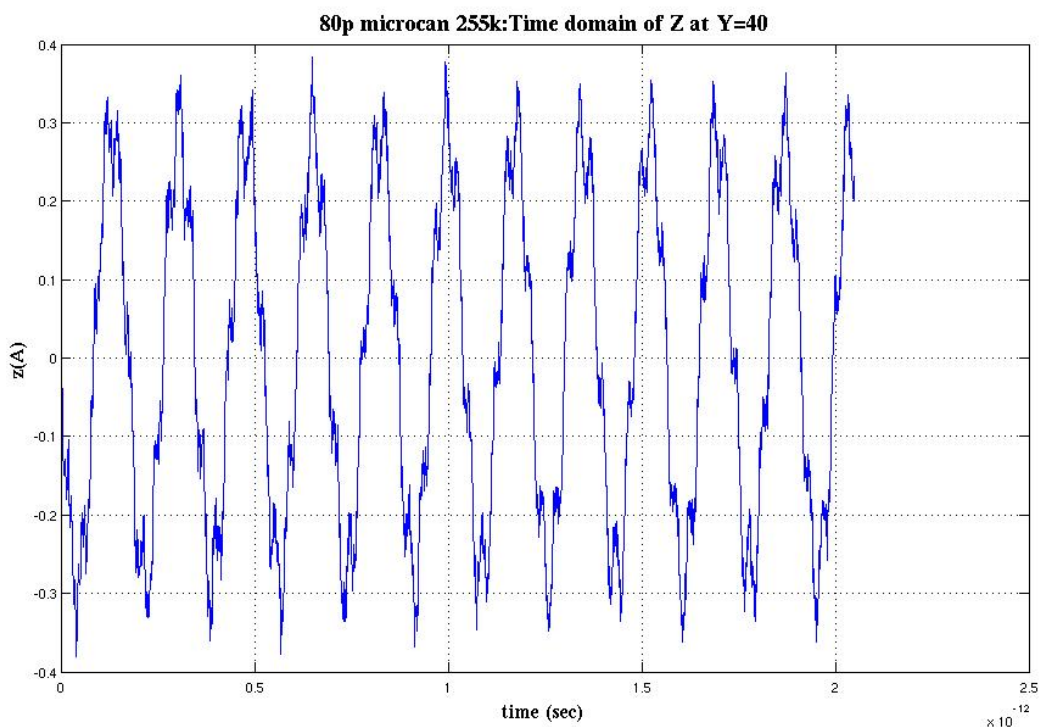


80, 100 and 120 periods respectively.

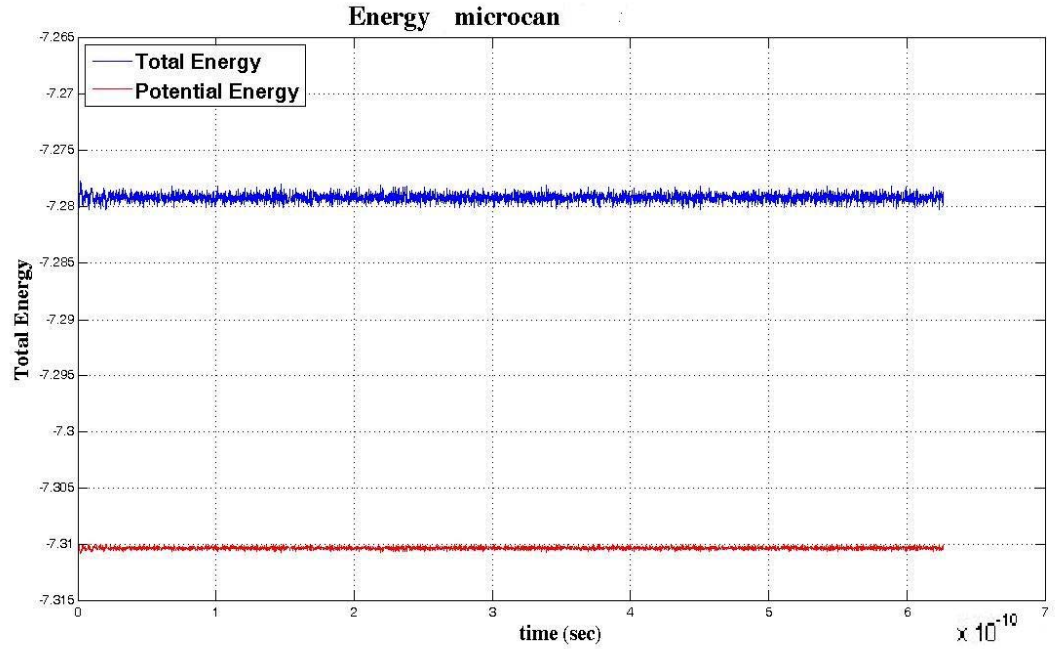
We also analyzed the error (difference) between the “old” analytical model and my results and plotted a graph of error as a function of the length of the nanotube for every mode, the results are presented in the figure bellow:



The vibration of Center of Mass of 167.24A nanotube in the Z direction:



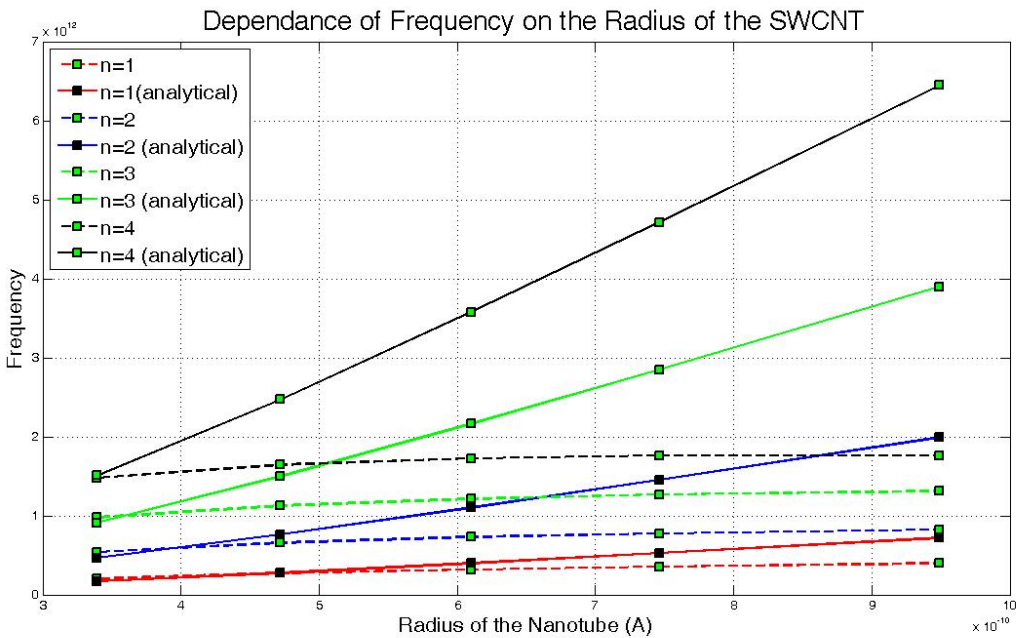
2. The energy changes as:



3. We also calculated the same parameters for the 98.38A nanotubes with different radii:

(5,5) R = 3.39A, (7,7) R = 4.75A , (9,9) R = 6.10A, (11,11) R = 7.46A and (14,14) R = 9.49A.

The results are presented below:



Future Plans

Our next step in the future will be a test of different boundary conditions. For example, it would be interesting to follow the frequency changes if instead of the nanotube being clamped at both ends (3 periods at each end) only the atoms, which are supposed to be connected to the surface, would be frozen. In later stages, in order to study the external energy loss mechanisms, we will connect the nanotube to the

silicon surface at the edge (see Fig. 1 or Fig. 8) by non-covalent bonds and monitor the changes in energy, frequencies and the quality factor of the system. In this part of the research electronic effects play an important role and need to be studied using *ab initio* models. Our previous experience in the electronic structure calculations could be very useful for this purpose. Some additional numerical experiments will also be carried out. To study the influence of the boundary conditions on the Q we will follow the changes in the angle between the nanotube and the silicon surface as is shown in Fig. 8.

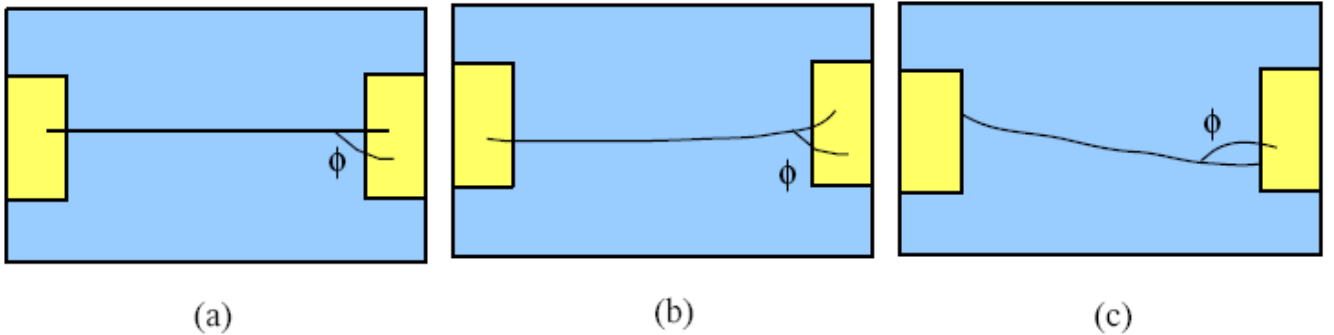


Figure 8. Suspended Single Walled Carbon Nanotube, showing optional angles (a) - (c) between the nanotube and the surface (yellow area).

In the experimental work the nanotube was suspended between two electrodes, the gate voltage was applied and caused an electrical force downward on the nanotube. Since the nanotube has an extremely high Young's modulus ~ 1 TPa it was deformed as a result of the applied force and the frequencies of the vibrational modes were changed, one of the most important questions is how the frequencies were changed and what is the effect of such a change on the quality factor? In order to answer these questions we will study the tensioned nanotube: we will expose the nanotube to the external forces in Z and Y directions as shown in Fig. 9.

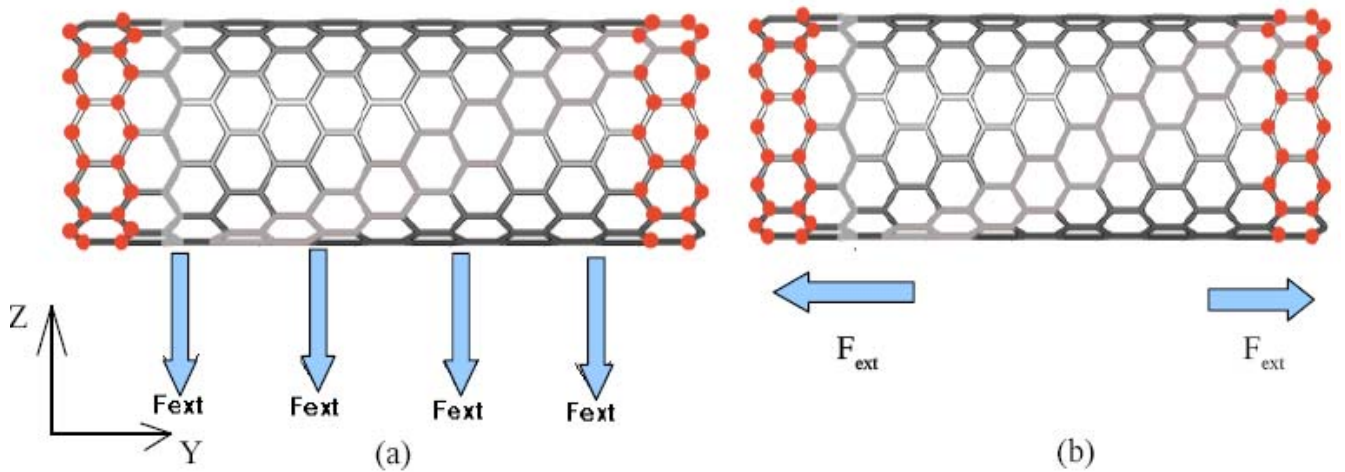


Figure 9. Suspended Single Walled Carbon Nanotube: (a) external forces acts in the direction opposite to the Z direction; (b) under tension in Y direction.

Another of the planned actions is to simulate one of the applications of the Single Walled Carbon Nanotube NEMS by adsorbing a small molecule onto the nanotube and monitoring the frequency shift to calculate the mass of the attached molecule.

Suspended Silicon Nanowires

In order to test different aspects of vibrational modes in NTs we decided to fabricate also silicon nanowire (SiNW) resonators. They have some similarities with NTs and can be tested with the same setups. First we had to fabricate such field effect transistor devices. We study how to make optimal metallic contacts to these wires, their electrical performance, and their dependence on doping parameters.

We have studied the influence of the RTA procedure on our pre-grown SiNWs, finding the optimized conditions for the silicide contacts formation in a systematic manner.

Nickel silicide formation is one of the most effective ways to control and improve the contacts in silicon NWs. A two step annealing process is a very effective way to make reliable and low resistance.

The first annealing step between 200–300 °C forms Ni_2Si with low diffusion rate but high resistance, while the second step between 400 and 450 °C is required to form low resistance NiSi with $\sim 0.6 \mu\text{m/sec}$ diffusion rate of the silicide along the wire.

To explore the influence of the RTA temperature on the transport behavior, the two steps RTA approach was repeatedly executed, where the temperature of the second RTA step was raised in 50 ° up to 450 °C.

To estimate the impact of the separated RTA steps, R_{on} (2 probes channel resistance taken from the saturated current of the strongly accumulated NW) was extracted.

Typically, for a constant S/D voltage when the swing voltage of the gate is considerably increased, the current start to saturate. The main reason for current saturation is ascribed to the serial contacts resistance whereas the silicon channel impedance itself is relatively negligible for such a high gate bias. The external contacts resistance can be estimated by plotting $V_{ds}/I_d = R_{on} = R_{NW} + R_{ext}$ as a function of $1/(Vg-V_T)$. Alternatively, one can extracts R_{on} by dividing the applied bias, V_{ds} , with the saturation current which is acquired at the highest gate voltage (figure 1, red circles).

In addition, in the case of a reliable ohmic contact, one can expect no dependence between R_{on} and V_{ds} , while for a rectifying contact the resistance should varied.

Namely, the low contact resistance should maintain for a large range of V_{ds} biases.

Under these criterions more than 35 devices were examined, 5 up-to 8 devices for each RTA step. Only devices with clear gate dependence that can be firmly opened and closed were taken into the statistics. Figure 2 summarizes the results of the average 2-probes resistance versus the annealing temperature for constant bias of $V_{ds}= 0.8 \text{ V}$.

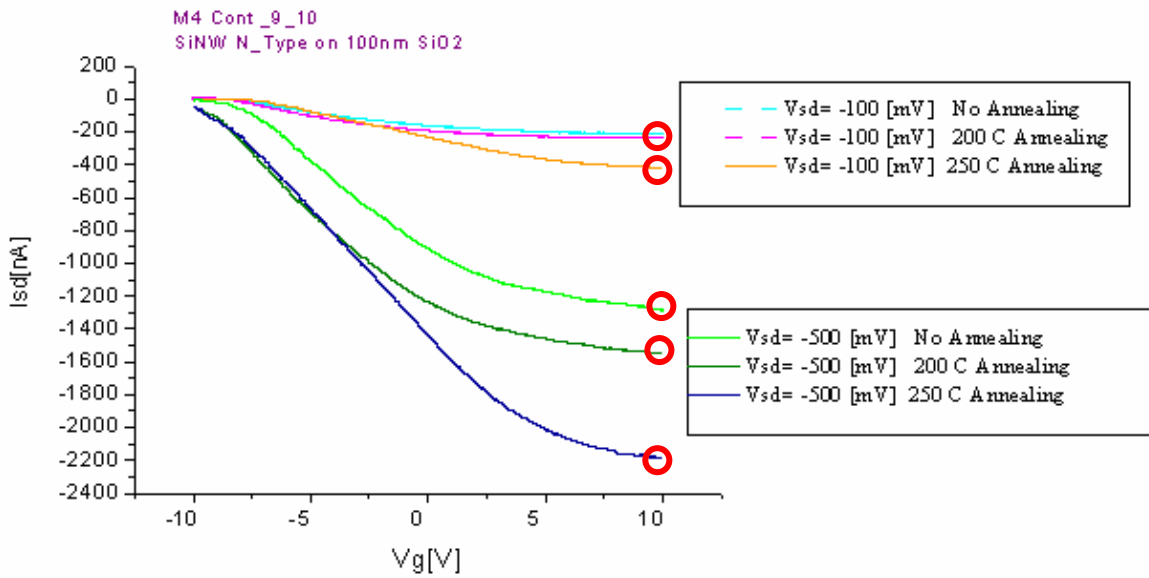


Figure 1 : I_{ds} Vs. V_g at $V_{ds} = -0.1$ and -0.5 V for different RTA procedures: no annealing, 200 and 250 °C. The red circles mark the saturation current of the strongly accumulated NW, for R_{on} extraction.

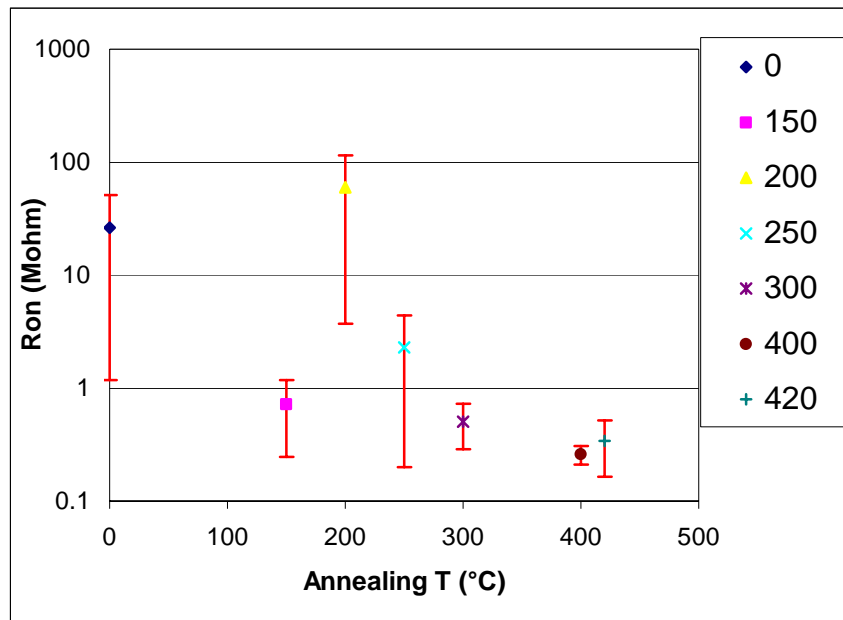


Figure 2 : R_{on} Versus the temperature annealing for constant bias of $V_{ds} = 0.8$ V. The red bars represent the standard deviation at each temperature.

The clearest improvement in R_{on} was obtained around 400-420 °C.

Moreover, the results exhibit a minor variation between different devices with typical resistance around 250-350 KΩ, reaching to the lowest resistance of 170 KΩ.

Further increase of the RTA temperature impaired the contact performances and deformed the NW shape.

Also, we discovered that for a short period of RTA (~10 to 15 sec) at 420°C, a reliable NiSi contact was formed with negligible silicide extensions of ~50nm, which is relatively insignificant in compare to the 1 μ m NW's channel length.

It should be mentioned that the interface between the silicide and the silicon appear to be sharp with no segmentation or nickel contamination in the SiNW midsection.

Accordingly, 15 sec at 420°C RTA procedure was chosen as the conventional annealing process for manufactured back-gate devices.

For transport measurements, more than 30 phosphorus-doped (n-type) SiNW devices where fabricated and their electrical characteristics were assessed. Figure 3 shows typical I_{ds} current versus drain-source voltage for 28 nm diameter and 1.6 μ m length (in-between the S/D) SiNW.

Examination of individual I_{ds} vs. V_{ds} curves shows that the current begins to saturate at positive but not negative values of V_{ds} and the conductance increases (decreases) as V_{gs} becomes more positive (negative). The saturation and V_{gs} dependence are characteristics of accumulation-mode n-channel FET, and thus demonstrate that the phosphorous has been incorporated as active donor-dopant in the SiNW.

In addition, I_{ds} vs. V_g (figure 4) curves exhibit high on-currents that reach to more than 4 μ A and relatively high transconductance of ca. 600 nS (for $V_{ds} = 1$ V). Furthermore, the SiNW device can be firmly depleted and the current can be cutoff efficiently. The full on/off current ratio determined from logarithmic plot is greater than 10^4 where the sub-threshold slope is about ~1000 mV/decade.

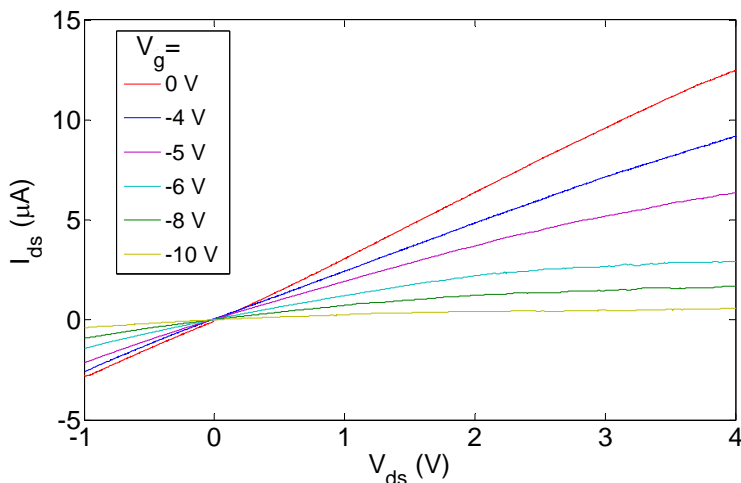


Figure 3 : Typical I_{ds} versus V_{ds} curves of 28 nm diameter and 1.6 μ m length n-type SiNWs, The back-gate voltage for each curve is indicated.

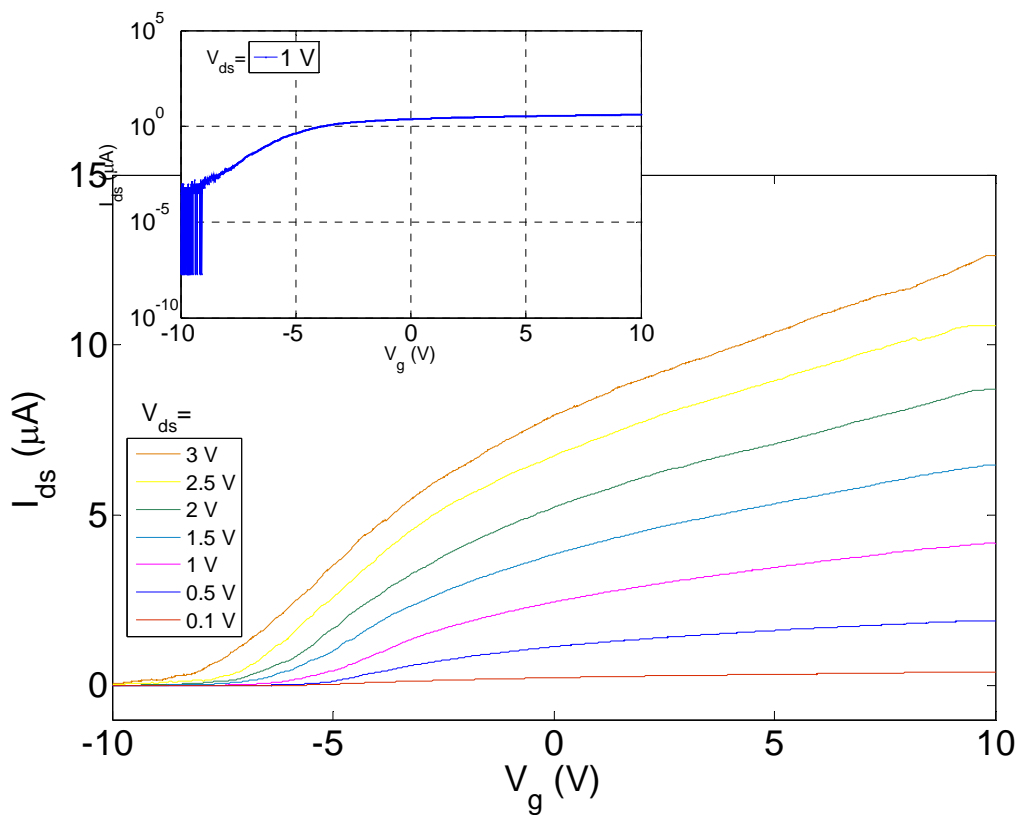


Figure 4 Typical I_{ds} versus V_g curves of 28 nm diameter and 1.6 μm length n-type SiNWs, V_{ds} voltage for each curve is indicated. Insert shows the logarithmic scale plot of I_{ds} versus V_g measured at $V_{ds}=1$ V, presenting on/off ratio $> 10^4$ and sub-threshold slope of ~ 1000 mV/decade.

Equivalently, 20 boron-doped (p-type) SiNW devices were fabricated and their electrical characteristics were assessed. Typical transfer characteristics are presented in figures 5-6.

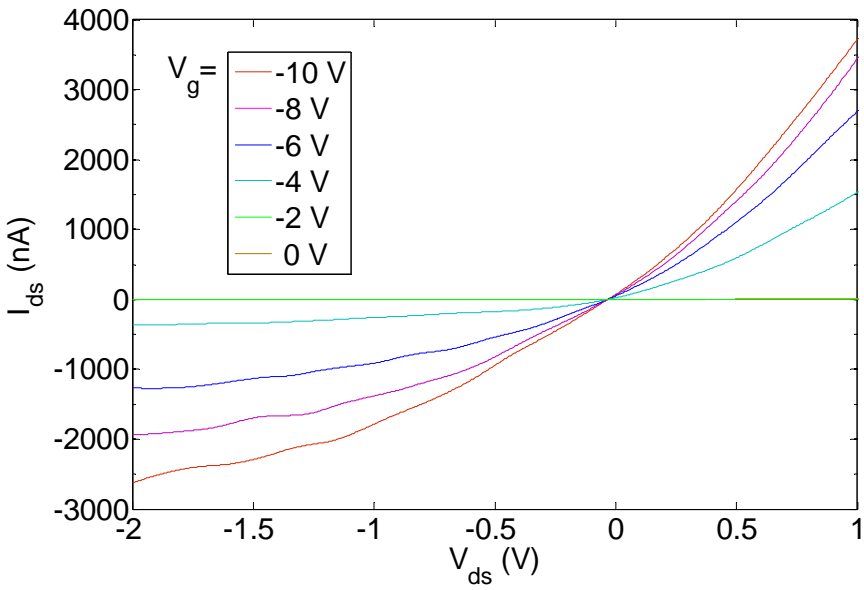


Figure 5 : Typical I_{ds} versus V_{ds} curves of 36 nm diameter and 2.4 μm length p-type SiNWs, The back-gate voltage for each curve is indicated.

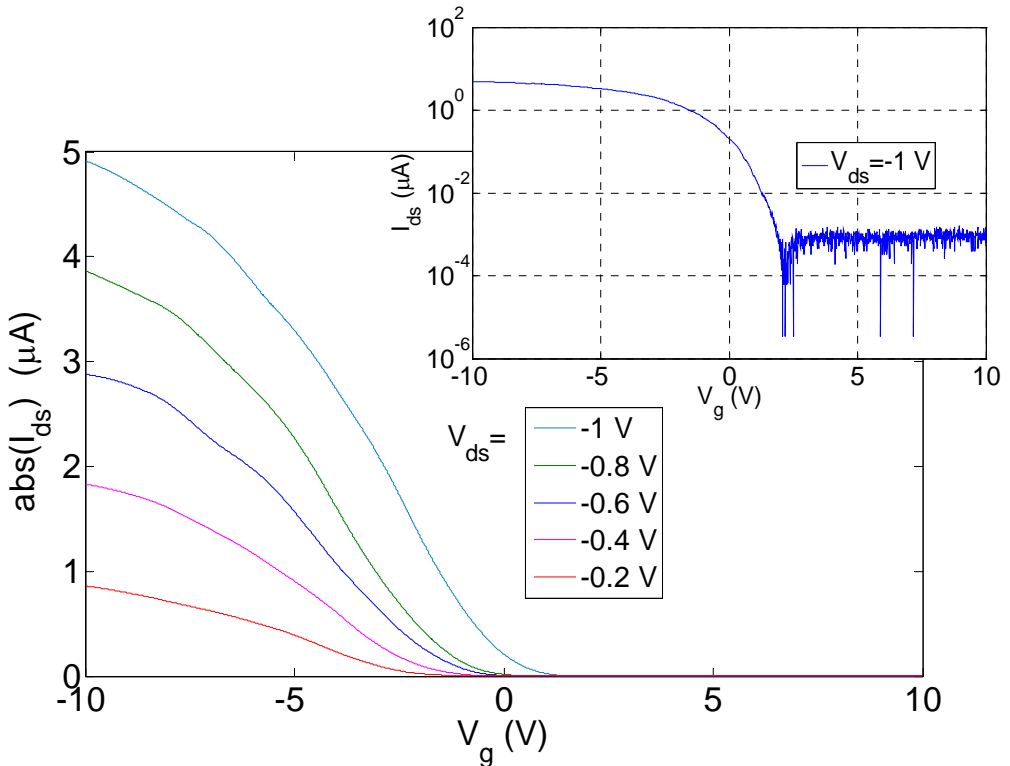


Figure 6 : Typical I_{ds} versus V_g curves of 36 nm diameter and 2.4 μm length p-type SiNWs, V_{ds} voltage for each curve is indicated. Insert shows the logarithmic scale plot of I_{ds} versus V_g measured at $V_{ds} = -1 \text{ V}$, presenting on/off ratio > 104 and sub-threshold slope of 450 mV/decade.

As can be seen in figure 5, the current begins to saturate at negative but not positive values of V_{ds} and the conductance increases (decreases) as V_{gs} becomes more negative (positive) as expected from the p-channel SiNW- FET. The extracted 2 probe resistance is about $230\text{K}\Omega$.

The I_{ds} vs. V_g curves exhibit high on-currents that reach to ca. $5 \mu\text{A}$ and high trans-conductance of 900nS (for -1 V V_{ds} bias).

The subthreshold slope is 450 mV per decade, which is a great improvement in regard to the slope of the n-type device. As before, the wire can be firmly depleted and the current can be cutoff with no observable ambipolarity behavior, yielding more than 10^4 on/off current ratio.

In general, p-type back-gate devices exhibited better consistency in their performance and provided superior results than the n-type.

To realize the differences between the two NW-FET types, statistics and histograms of the NW's key parameters were taken, where green and red colors indicate the n-type and the p-type frequent results, respectively. In addition, two colored arrows in each figure mark the average empirical result. All electrical characteristics data extracted from single NWs when biased at $|V_{ds}| = 1 \text{ V}$.

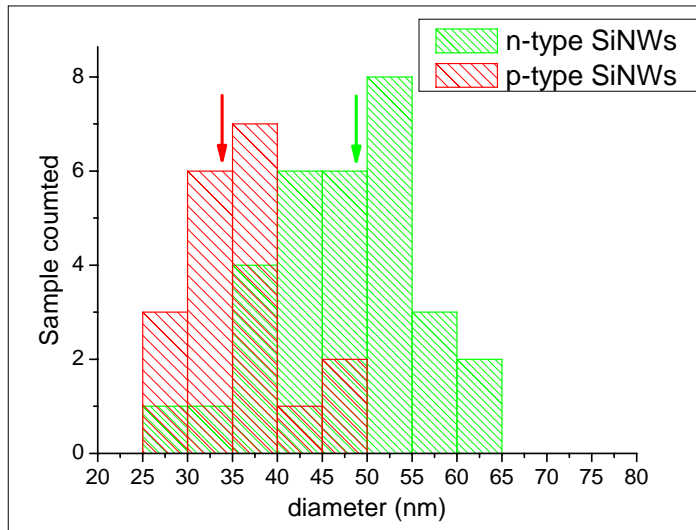


Figure 7 SiNWs diameters Histogram, extracted by AFM measurements, P-type NWs are mostly in between 30 to 40 nm while N-type NWs are in between 40 to 55 nm. The average thicknesses are 34 and 48 nm for p-type and n-type, respectively.

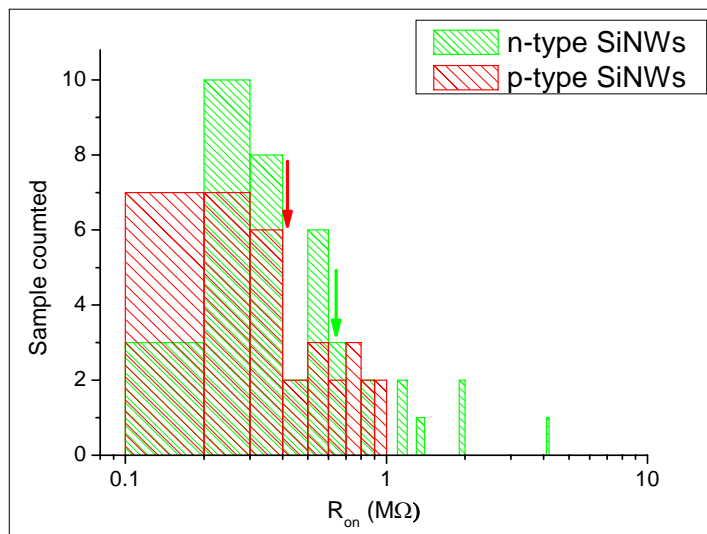


Figure 8 Histogram of Ni-contacted SiNWs resistance determined by 2-probe measurements, the average resistances are $430\text{ K}\Omega$ and $640\text{ K}\Omega$ for p-type and n-type, respectively.

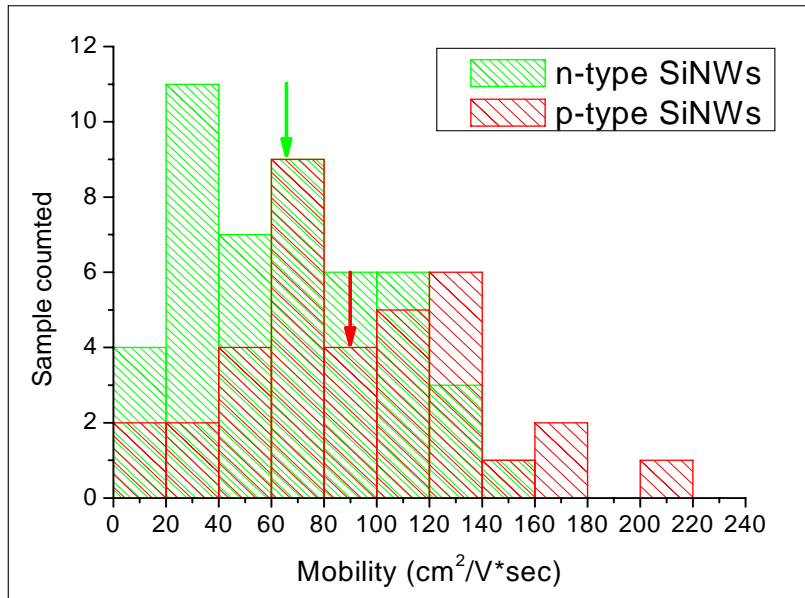


Figure 9 Histogram of SiNWs mobility valued from the max transconductance in the linear zone, exhibiting high effective mobility with average of 91 and 65 $\text{cm}^2/\text{V}\cdot\text{sec}$ for p-type and n-type NWs, respectively.

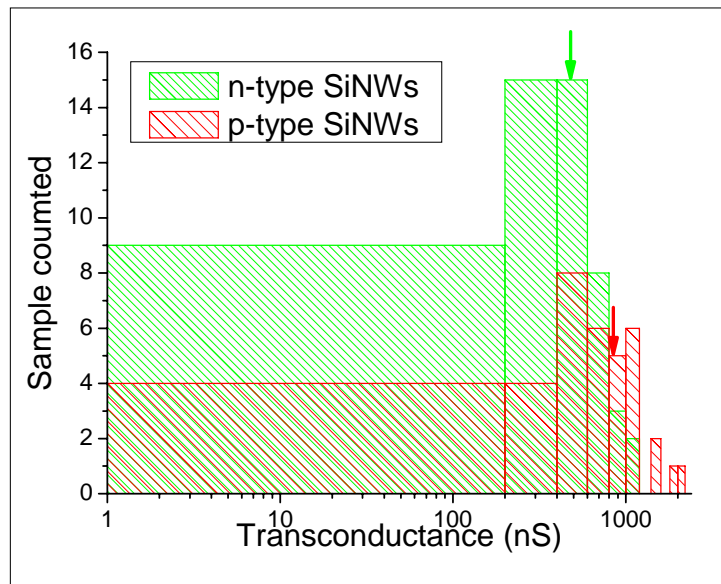


Figure 10 Histogram of the transconductance (g_m) taken from the maximum slope of the linear zone of the I_d - V_g curves. The average results are 820 and 475 nS for p-type and n-type NWs, respectively.

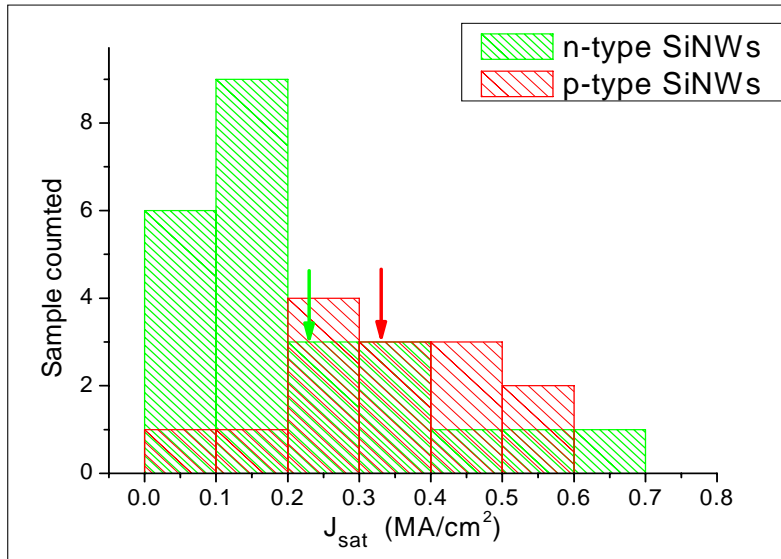


Figure 11 Histogram of the max-current density (J_s) extracted from electrical characteristics in the on-state divided by the NW cross-section. The average results are 0.33 and 0.23 MA/cm^2 for p-type and n-type NWs, respectively.

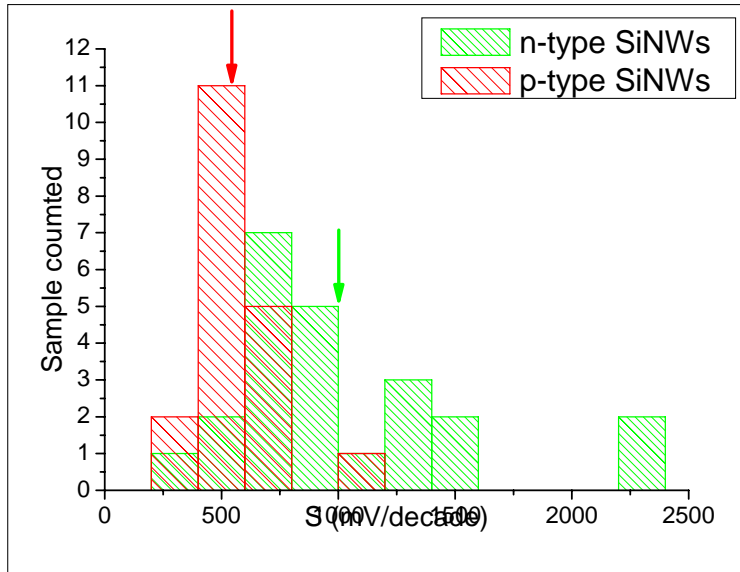


Figure 12 Histogram of the sub-threshold slope for the 100 nm oxide back-gated devices, the average slopes are 545 and 1000 mV/decade for p-type and n-type NWs, respectively.

The superiority of p-type devices in comparison to the n-type is evident in all extracted electrical characteristics. The result might be surprising since in bulk silicon the electron mobility is higher than hole. But, taking into account the NWs diameters (where p-type found to be ~ 15 nm thinner than the n-type NWs in average) and the higher built-in Schottky barrier for the n-type wires, the present situation can be more understandable. What is more, examination of the growth conditions of this two n/p NWs batches confirmed that the doping concentration of the n-type wires are

considerably lower than the p-type, a factor that can cause to another derogation of the electron injection ability through the SB contacts.

To summarize, Table 1 presents some key characteristics of our devices in compare to state-of-the-art, back-gated SiNWs reported in recent years.

Table 1 : Comparison of state-of-the-art, back gated SiNW-FETs.

	this work	this work	Cui nano letter 2003	Zheng Adv. Mat
	p-SiNW	n-SiNW	p-SiNW *	n-type lightly doped
	0.8-3.3	1-4	0.8-2	1-2
em] ection	30-40 (34)	40-55 (48)	10-20	(~20)
uration	-1	1	-1	1
leted	yes	yes	yes	no
current	up-to 10^6	up-to 10^6	$10^4 >$	$10^4 >$
$\text{nm}^2]$	0.1-0.6 (0.33)	0.04-0.57 (0.23)	0.32-1.2	~0.5
	0.17-1.2 (0.43)	0.2 - 4.12 (0.64)	0.1 - 10 (0.62)	~1
	20-220 (91)	20-154 (65)	230-1350 (560)	(50) **
.	this work	this work	Cui nano letter 2003	Gengfeng Adv. Mat
	p-SiNW	n-SiNW	p-SiNW *	n-type lightly doped
ctance	270-2020 (820)	80-1130 (475)	340 - 2000 (800)	100-1500 (400)

old ade]	320- 1000 (545)	370- 2200 (1000)	174- 609	~300
	NiSi	NiSi	Ti/Au	NiSi

* After passivation of oxide defects by chemical modification

** The average mobility is $260 \text{ cm}^2/\text{V*sec}$ after subtraction of the contacts resistance

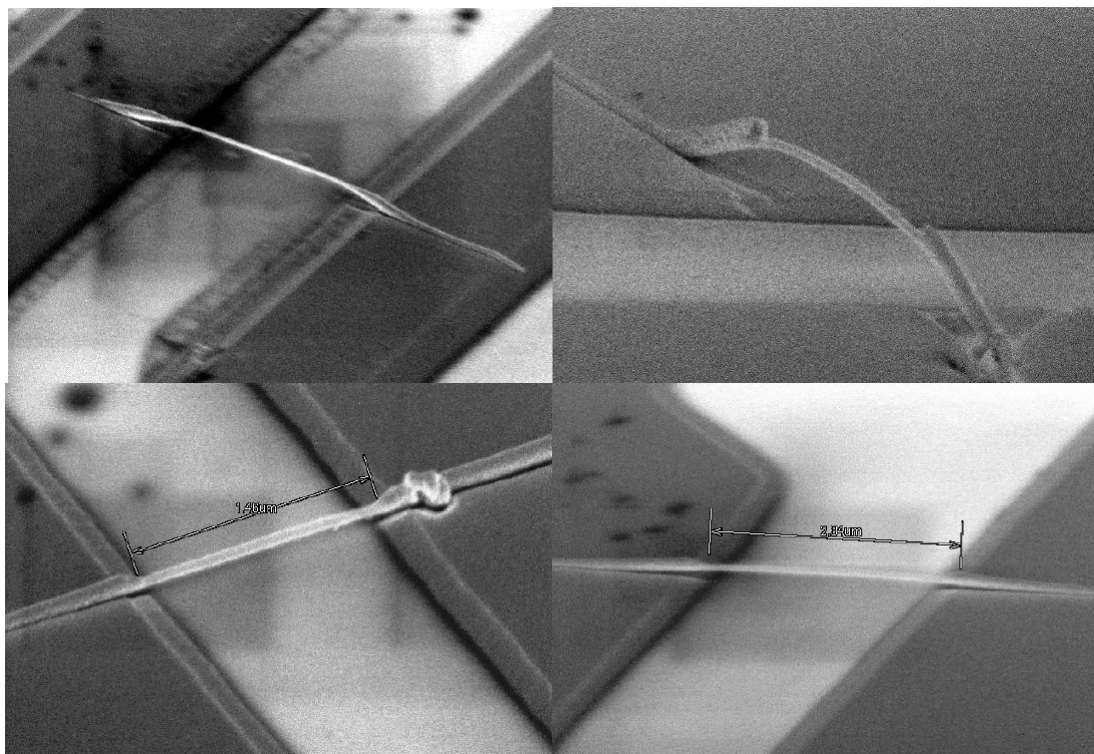
The electrical characteristics of the fabricated back-gate devices are quite resembled to the previously reported achievements.

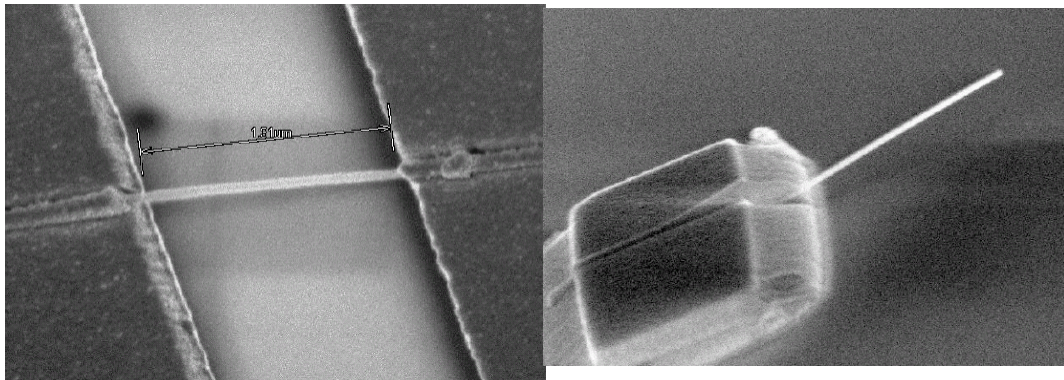
The new SiNWs-FETs exhibit the same magnitude of high on-current and transconductance which are essential to high-speed electronics.

In addition, transport behavior exhibits high free-charge mobility ($\sim 100 - 150 \text{ cm}^2/\text{V sec}$) which is comparable to the technology of planer SOI (silicon on insulator) FETs.

The high on-off current ratio with the relatively low capacitance of the NWs ($\sim 1 \text{ fF per } 1\mu\text{m SiNW}$) suggested that these NW-FETs are suitable for low-power applications.

Equipped with SiNW transistors we developed novel technique to fabricate suspended devices with minimum contamination of the wires themselves. This approach is crucial in order to achieve higher quality factors. Below are pictures of various suspended oscillators that we have fabricated. One can identify doubly clamped wires, bent wires, free cantilevers, etc...





Tilted SEM images of different crossbeams and cantilevers made of SiNWs, illustrating the great variety of structures that can be produced by the new fabrication technique. Different contacts configuration yields diverse built-in strain in the crossbeams.

Having these resonators in hand enable us to study influence of dissipation processes that are mutual to NTs and SiNWs, and ones that are of different origin. We expect that boundary conditions and anchoring points will play a major role in both resonators, but tension and phonons distribution will have completely different influence.

Static Deformation:

One popular method to characterize Young modulus and built in tension is to utilize force curve measurements with Atomic Force Microscope (AFM).

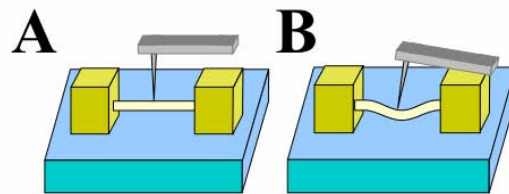
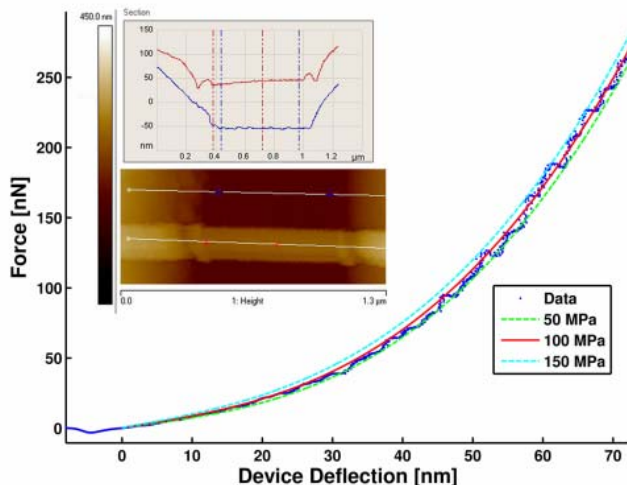


Figure 1: Schematic of the SiNW beam, clamped by an embedding metallic contact, subjected to a point force inflicted by an AFM tip. **A** The beam prior to bending; **B** The beam during bending test. The total descend is the sum of the NW deflection and the cantilever deflection.

Acquire force curve measurements yield the following graph

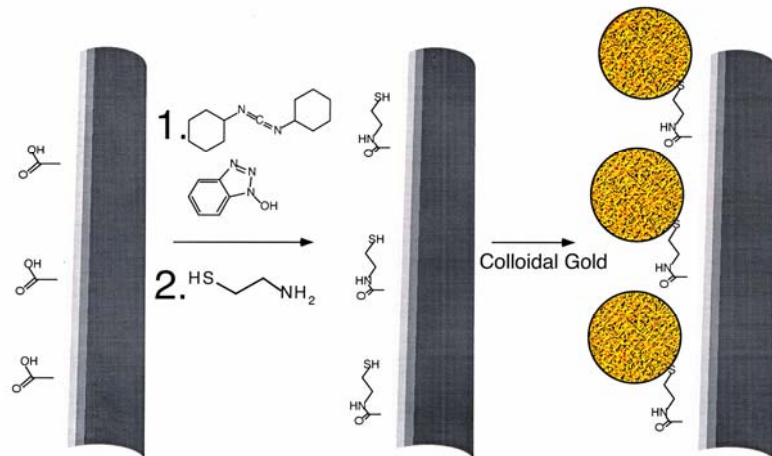


from which one can extract the wire Young Modulus and built in tension. For the example above, the residual stress is 100MPa and $Y=170\text{GPa}$, in good agreement with theoretical values.

Having the static properties of these wires, one can estimate their dynamical behavior, and more specifically their resonance frequencies.

Chemical Functionalization -

An important ingredient of this research proposal is the attachment of the small mass to the surface of NTs or SiNWs. The attachment can be very rigid and strong, as covalent bonding, but can be also looser, like Van der Waals interaction. Covalent bonding requires intensive research even before the final device is available. Therefore we decided to use amine chemistry in order to attach small molecules onto the 1-dimesional wires. NTs contain carboxylic acid (COOH) groups on their surrounding. Thus, one should have amine group connected to the attached molecule in order to achieve covalent bond between it to the NT. For that purpose, we tested attachment of gold colloid to the surface of NT. We exploit amine chemistry (utilized Dicyclohexylcarbodiimide (DCC) and 1-Hydroxybezotriazole (HOBT)) and attached gold colloid with aminoethanethiol. Figure 13 presents the chemical flow of this reaction. Since the gold colloids are visible with SEM and AFM, we could examine our chemical functionalization with great details. Figure 14 depicts success of such chemical attachment over the exterior surrounding of NTs. Functionalization of SiNWs is currently under process.



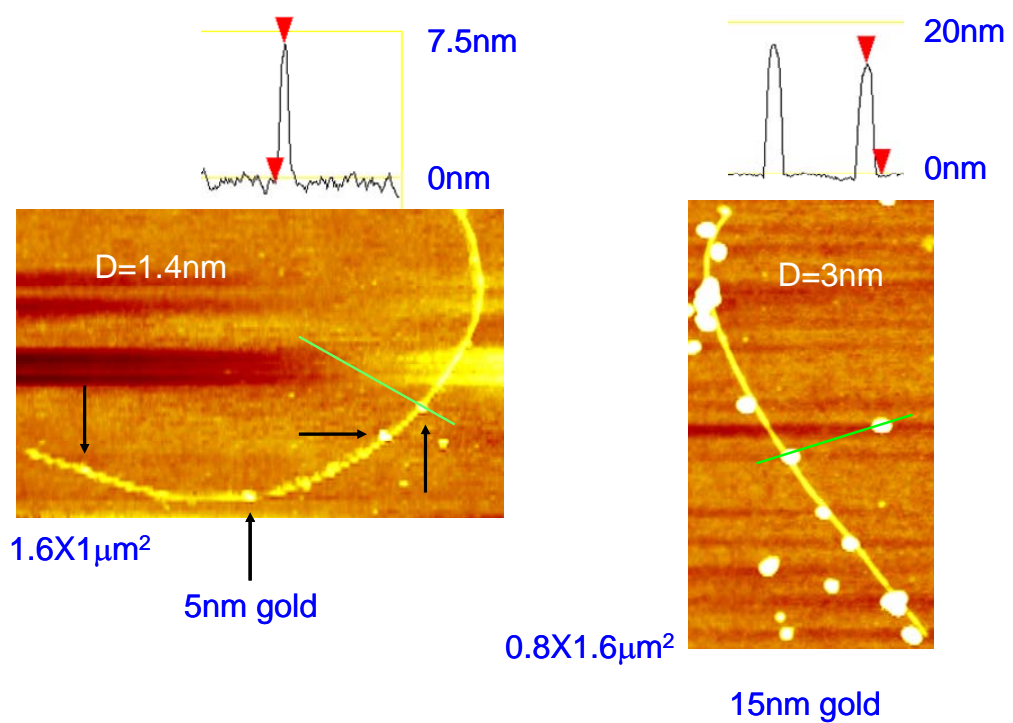


Figure 14: AFM images of gold colloids (5nm and 15nm) covalently attach to NTs.

References

1. K.L. Ekinci, Y.T. Yang, M.L. Roukes, J. Appl. Phys., 95, 5, 2682 (2004).
2. B. Illic, Y. Yang, K. Aubin, R. Reichenbach, S. Krylov and H.G. Craighead, Nano Lett., 5, 925 (2005).
3. A.N. Cleland, M. Poprathic, I. Ferguson, Appl. Phys. Lett, 79(13), 2070 (2001).
4. V. Sazonova, Y. Yaish, H. Ustunel, D. Roundy, T. A. Arias, and P. L. McEuen, Nature 431, 284 (2004).
5. D.W. Brenner, Phys. Rev. B 42, 9458 (1990).
6. K. L. Ekinci, M. L. Roukes, Rev. Sci. Instrum. **76**, 061101 (2005).